Available online at www.sciencedirect.com
SCIENCE DIRECT
Journal of volcanology and geothermal research
ELSEVIER
Journal of Volcanology and Geothermal Research 150 (2006) 244–269
www.elsevier.com/locate/jvolgeores

A four-dimensional viscoelastic deformation model for Long Valley Caldera, California, between 1995 and 2000

Andrew V. Newman [a,*], Timothy H. Dixon [b], Noel Gourmelen [b]

[a] *Earth and Environmental Sciences, Environmental Geology and Spatial Analysis (EES-9), Los Alamos National Laboratory, Los Alamos, NM 87544, USA*
[b] *Rosenstiel School of Marine and Atmospheric Science, University of Miami, 4600 Rickenbacker Cswy., Miami FL, 33149, USA*

Received 11 June 2004; received in revised form 24 September 2004
Available online 11 November 2005

Abstract

We investigate the effects of viscoelastic (VE) rheologies surrounding a vertically dipping prolate spheroid source during an active period of time-dependent deformation between 1995 and 2000 at Long Valley caldera. We model a rapid magmatic inflation episode and slip across the South Moat fault (SMF) in late 1997. We extend the spherical VE shell model of Newman et al. [Newman, A.V., Dixon, T.H., Ofoegbu, G., Dixon, J.E., 2001. Geodetic and seismic constraints on recent activity at Long Valley caldera, California: Evidence for viscoelastic rheology. J. Volcanol. Geotherm. Res. 105, 183–206.] to include a prolate spheroid geometry more accurately representing the probable source geometry inferred from other studies. This paper presents the first attempt to geodetically constrain the volcanic deformation source volume at Long Valley, a parameter for hazard assessment. Including fault slip along the SMF explains significant deformation observed with several EDM baselines and components of two continuous GPS time series. Additionally, the model explains the spatial extent of deformation observed by InSAR data covering the 1997–98 inflation episode. For the time period studied, the VE model requires modest pressure changes (maximum of 14.3 MPa) that are far lower than the overburden pressure (~115 MPa), and less than the maximum for a purely elastic model with the same geometry and elastic strength (~45 MPa). Thus, the inclusion of a realistic VE component significantly lowers the inferred pressures necessary to explain observed surface deformation. Though our model is non-unique, it is consistent with a broader variety of data compared to purely elastic models. Only right-lateral slip, and not dilitation, was necessary to explain offsets in EDM data near and crossing the SMF.

Keywords: global positioning system; finite element analysis; Long Valley Caldera; viscoelasticity; magma chambers

1. Introduction

Long Valley Caldera is situated in east-central California on the eastern edge of the Sierra Nevada

* Corresponding author. Present address: School of Earth and Atmospheric Sciences, Georgia Institute of Technology, Atlanta, GA 30332, USA. Tel.: +1 404 894 3976; fax: +1 404 894 5638.
E-mail address: andrew.newman@eas.gatech.edu (A.V. Newman).

0377-0273/$ - see front matter © 2005 Elsevier B.V. All rights reserved.
doi:10.1016/j.jvolgeores.2005.07.017

range (Fig. 1). The 17×32 km^2 caldera was created approximately 760,000 yr ago in a large ignimbrite eruption, expelling more than 600 km^3 of pyroclastic material and ash that also formed the locally >1 km thick Bishop tuff (Bailey et al., 1976). Shortly after caldera formation, the central resurgent dome formed from magmatically induced uplift and coincident lava flows, rising approximately 500 m above the caldera floor.

In the last 40 k.y. eruptions have been isolated to the Inyo–Mono chain, running north-south from the western part of Long Valley Caldera to Mono Lake (Fig. 1), and consisting predominantly of rhyolitic–rhyodacitic flows (e.g., Miller, 1985; Fink, 1985; Vogel et al., 1989). The most recent eruptive period was between 700–500 yr ago along the length of the Inyo–Mono chain and ~200 yr ago in Mono Lake, occurring in a series of small eruptions and phreatic explosions (Miller, 1985).

Starting between 1978 and 1980 and continuing to present, the Long Valley region has experienced seismicity and surface deformation well above background levels. The most active period of inflation occurred between 1978 and 1984, with four M~6 earthquakes and ~40 cm of inflation centered on the resurgent dome (Hill et al., 1991; Langbein et al., 1993, 1995). Between 1990 and mid-1997, background seismicity and slow inflation continued, then exponentially increased in late 1997, before exponentially decaying to a point of zero growth by mid-1998 (Figs. 2 and 3). The change from exponential increase to decrease coincided with a maximum in South Moat seismic moment release, suggesting that resurgent dome inflation and South Moat seismicity are directly linked (Fig. 5 in Newman et

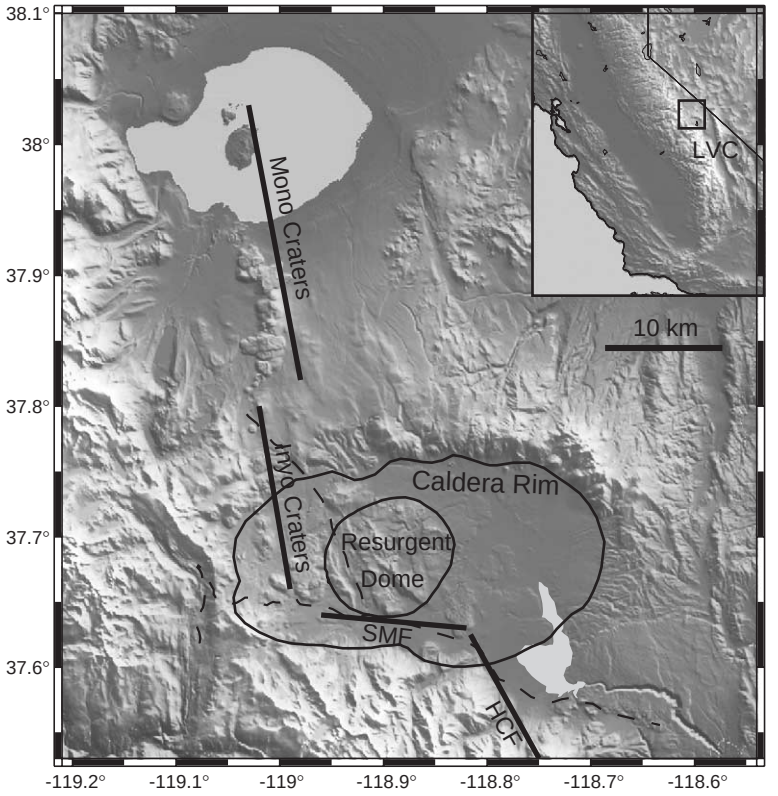

Fig. 1. Topographic image of the Long Valley Caldera (LVC), the central resurgent dome and the Inyo and Mono chains from the 7.5′ USGS National Elevation Database. The caldera rim shown here and in subsequent figures is the topographic rim which is likely to be considerably larger than the geologic caldera rim. Also shown are the South Moat Fault (SMF) and Hilton Creek Fault (HCF). Inset shows the location of Long Valley in the eastern Sierras.

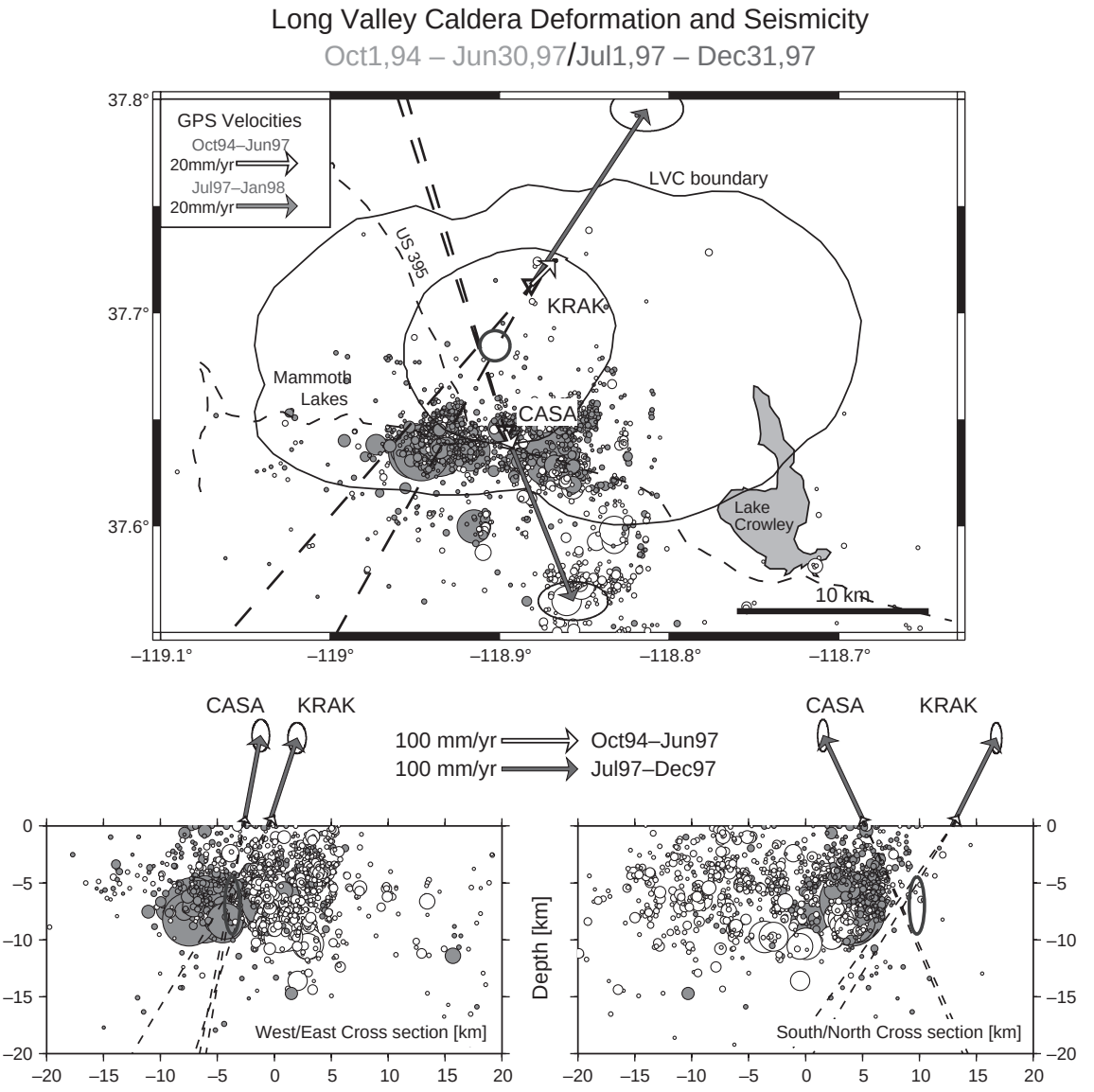

Fig. 2. (Top) GPS deformation and seismicity at Long Valley Caldera in eastern California for two different time periods (Newman et al., 2001). GPS deformation rate relative to Sierra Nevada block (arrows with 95% confidence ellipses; errors for early period are almost imperceivable) and seismicity scaled by magnitude (circles) shown for low activity period with open symbols (1 October 1994–30 June 1997), and high activity period with filled symbols (1 July, 1997–31 December, 1998). Dashed lines show the projected intersection point for GPS data. Open thick ellipse shows 95% confidence limits of shallow deformation source location for the period 1989–1992 described by Langbein et al. (1995). Seismic data were collected and analyzed by the Northern California Earthquake Data Center. (Bottom) Same data as above for south/north and west/east cross-sections.

al., 2001; Hill et al., 2003). The seismic and inflationary activity during this most recent phase of unrest almost certainly reflect intrusion of basaltic magma from the upper mantle and/or lower crust into the middle and upper crust (Dvorak and Dzurisin, 1997; Battaglia et al., 1999, 2003b).

In Newman et al. (2001) we examined this phase of unrest using a model that incorporates a constant

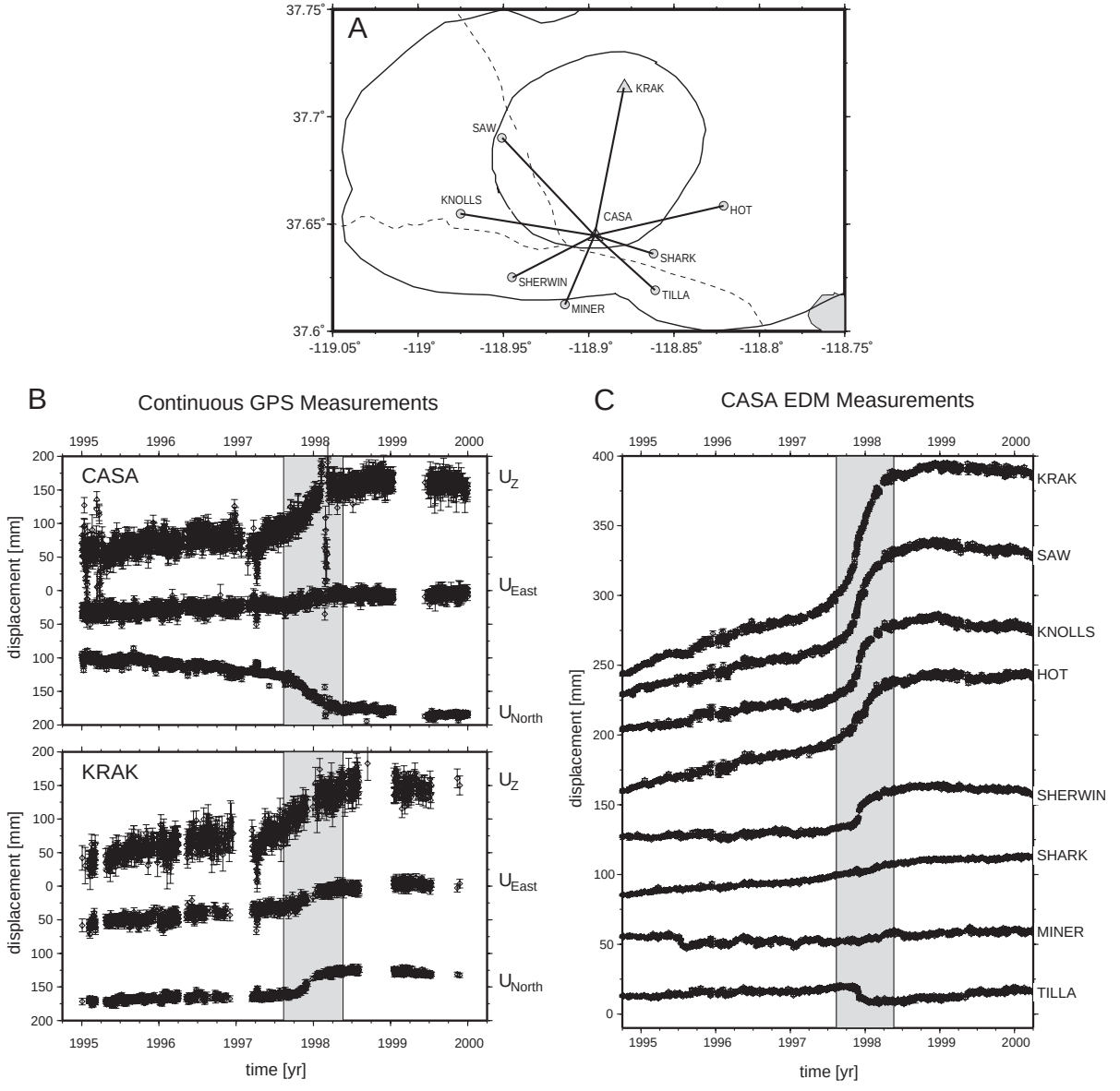

Fig. 3. (A) Location of continuous GPS sites (triangles) and EDM baselines measured from site CASA (lines) used in this study. (B) Daily GPS vertical, east and north positions with 1σ error estimates relative to stable Sierra–Nevada Block for continuous sites CASA and KRAK spanning the resurgent dome. The long-term steady change in positions between 1995 and early 1997, shows slow growth of the resurgent dome before the highly active period in late 1997–early 1998. Gray bar represents period of deformation captured by InSAR pair (Pair A) in Fig. 4. (C) Near-daily EDM measurements taken from the laser base station at CASA (next to continuous GPS site CASA) and 8 individual reflectors spanning the resurgent dome and South Moat. CASA–KRAK EDM is nearly identical to baseline measured by GPS for those sites (Newman et al., 2001).

thickness Maxwell viscoelastic (hereafter VE) shell surrounding a small spherical magma chamber, and compared these results with Electronic Distance Measurements (EDM) from the baseline CASA–KRAK, the line spanning the resurgent dome with the largest signal to noise ratio. The model devel-

oped in Newman et al. (2001) was the first to compare observed volcanic deformation with predictions that incorporated VE rheology.

Vertically dipping prolate spheroid pressure sources have also been used to describe the 1997–1998 Long Valley deformation (Tiampo et al., 2000; Fialko et al., 2001; Battaglia et al., 2003a; Langbein, 2003). Here we again examine the 1997–98 phase of unrest, using a vertically dipping prolate spheroid pressure source, surrounded by a 0.5 to 1.0 km thick VE shell within a purely elastic half-space plus earthquake-induced deformation along the south moat, and compare the predictions to multiple geodetic data types. We estimate the minimum plausible source volume by making the assumption that the pressure within the source cannot exceed lithostatic load. We compare these results to 6 years of data from eight single-component EDM lines, two three-component continuous GPS receivers on the resurgent dome, and two Interferometric Synthetic Aperture Radar (InSAR) images spanning the most significant inflation period.

2. Data

The increased seismic activity and notable elevation changes in leveling data between 1978 and 1982 motivated the USGS and other agencies and universities to begin intensely studying the Long Valley region. Geophysical instrumentation included short period and broad band seismometers, a two-color EDM network, volumetric strain meters (dilatometers), tiltmeters, campaign GPS (Dixon et al., 1993) and continuous GPS (Webb et al., 1995; Dixon et al., 1995, 1997) was later added. Seismic and geodetic information gathered from these instruments are useful for assessing location, intensity and type of local earthquake activity (e.g., Newman et al., 1997; Dreger et al., 2000; Prejean et al., 2003; Hill et al., 2003), developing low resolution images of subsurface rheology (e.g., Steck and Prothero, 1994; Sanders et al., 1995; Sanders and Nixon, 1995; Foulger et al., 2003, 2004), and defining the extent of surface deformation caused by both earthquake and volcanic sources (e.g., Langbein, 1989; Langbein et al., 1993, 1995; Thatcher and Massonnet, 1997; Tiampo et al., 2000; Fialko et al., 2001; Newman et al., 2001; Battaglia et al., 2003a; Langbein, 2003).

2.1. Geodetic data

In addition to the near continuously recorded GPS, daily EDM, tilt and strainmeter data, deformation at Long Valley is also measured through infrequent leveling (every 2–3 yr), frequent InSAR imagery (~1 per month depending on satellite), and less frequent, survey mode EDM at additional sites. Here we focus on available daily EDM, continuous GPS and InSAR data as they best capture the spatial and temporal deformation for the 1997–1998 inflation episode and intense seismic swarm activity.

2.1.1. GPS

Continuous GPS data were measured at two sites, CASA and KRAK, within the caldera and atop the resurgent dome during the 1997–1998 inflation episode (Fig. 2). The GPS data were analyzed at the University of Miami's Geodesy Laboratory following Dixon et al. (1997) and are further explained in Newman et al. (2001). The data are reduced in a global reference frame daily to yield geographic north, east and vertical components of deformation. The combination of white and flicker noise in the north, east and vertical components average ~7, 11 and 21 mm. Random walk error, probably representing monument noise, is ~2 mm/a$^{1/2}$ (Mao et al., 1999; Langbein and Johnson, 1997).

In order to investigate local deformation from the GPS data, we removed the effects of the North American plate (NAP) rotation in the International Terrestrial Reference Frame (ITRF) 2000 (θ_{NAP}, ϕ_{NAP}, ω_{NAP}=4.59°S, 82.91°W, 0.195°/ma) following Sella et al. (2002). Additionally we removed Sierra Nevada block (SNB) motion relative to NAP (θ_{SNB}, ϕ_{SNB}, ω_{SNB}=17.0°N, 137.3°W, 0.28°/Ma) following Dixon et al. (2000). By definition, there are no vertical components to NAP or SNB motions. After removing background tectonic motion, resultant vectors represent local deformation for Long Valley.[1] Fig. 3 shows the resulting time series for the vertical, east and north components for sites CASA and KRAK. Low rates of

[1] Though Long Valley is generally considered to be on a transition between SNB and stable NAP (e.g. Dixon et al., 2000), the removal of SNB motion appears to be correct here since the resulting GPS signal at CASA and KRAK can be mostly described by a single, radially symmetric inflationary source (discussed later).

deformation are observed through mid-1997, when all components for both stations show exponentially increasing displacement. Because the resulting vectors (Fig. 2) do not appreciably change direction with the rapid increase in magnitude, it is reasonable to assume that there is no significant change in the location or depth of the deformation source. Newman et al. (2001) noted that the source responsible for the steady inflation between 1995 through mid-1997 and the exponential change shown between mid-1997 through early 1998 did not show appreciable horizontal location or depth changes between 1989 and 1992 as defined within 95% confidence by Langbein et al. (1995) (Fig. 2).

GPS data provide continuous geocentrically referenced three-component vector displacement data. If uncertainties are small, two GPS stations are sufficient to define a point source within a homogeneous half-space (Dixon et al., 1997). However, because the true source of deformation has a finite volume, is likely non-spherical, and because the 1997–98 episode includes possible deeper sources and offsets along the South Moat, and involved rapid non-linear inflation and possible anelastic rheology, examination of other data such as EDM and InSAR is important.

2.1.2. EDM

EDM uses laser ranging to measure a single component length change between a base station and a series of reflectors. At Long Valley, a 2-color laser is used to minimize errors in length measurements due to atmospheric pressure and moisture. Per kilometer of baseline, white noise errors are between 0.1–0.2 mm. Random walk errors, which are reduced with recording time for steady deformation, are ~1.6 mm/$a^{1/2}$ (Slater and Huggett, 1977; Langbein and Johnson, 1997). At Long Valley Caldera, frequent (near daily) EDM measurements are made from a base site at Casa Diablo (CASA), next to the continuous GPS station of the same name, to eight reflectors (KRAK, SAW, KNOLLS, HOT, SHERWIN, SHARK, MINER and TILLA) (Fig. 3). Baselines are measured from CASA to nearly 30 additional sites between 4 and 15 times per year. Infrequent, annual to sub-annual measurements are made from another five base stations within the caldera and along the Inyo–Mono chain.

For this study we used the near-daily baselines measured from CASA and collected between 1998 and early 2000. While EDM data augment available continuous GPS with additional spatial coverage of continuous data, the data only provide a single component of relative motion between reflector sites and the base station. The time series of these data (Fig. 3) have lower errors and fewer outages than GPS data. Four baselines across the resurgent dome (KRAK, SAW, KNOLLS and HOT) all capture the long steady inflation between 1995 and 1997, before exponentially increasing then decaying in late 1997–early 98. The baselines which are near or cross the South Moat (SHERWIN, SHARK, MINER and TILLA) are less clear. Two of these sites (SHERWIN and TILLA), show a clear step in late 1997, with the TILLA baseline shortening, while the other two (SHARK and MINER) show a slow gradual increase or no clear length-change. This step in late 1997 is most likely due to active faulting across the South Moat (Langbein, 2003) and will be briefly explored in this study.

Though GPS and EDM can generate essentially continuous deformation data, they do not provide dense spatial coverage, necessary to fully define additional deformation sources or non-radially symmetric deformation. Spatially dense InSAR data can fill this gap.

2.1.3. InSAR

InSAR reveals phase differences between reflected radar signals off the surface of the earth and is well-suited for volcano deformation studies. The data are affected by topography, thus it is necessary to remove known elevation using a digital elevation model (DEM). The resulting phase differenced information gives length changes between individual points on the earth's surface in the line-of-sight (LOS) direction of the satellite. The information in adjacent pixels are highly correlated, and it is difficult to assess errors associated with individual pixels. We assume that errors in range change are approximately 10 mm (Moran et al., 2005-this issue).

The InSAR data were collected by the European Space Agency C-band satellite ERS-2, which has a wavelength of 56.6 mm and a repeat orbit every 35 days and were processed using the Caltech/JPL InSAR package, ROI_PAC. Fialko et al. (2001) stacked multiple image pairs to obtain an accurate estimate of average deformation between June 1996 and July 1998. However, in order to capture time-

dependent deformation, it is necessary to examine individual pairs. We examine two such pairs spanning the major inflationary 1997–98 episode (Fig. 4): Pair A—12 August, 1997 to 19 May, 1998; Pair B—25 November, 1997 to 19 May, 1998. Pair A covers most of the 1997–1998 deformation episode while pair B,

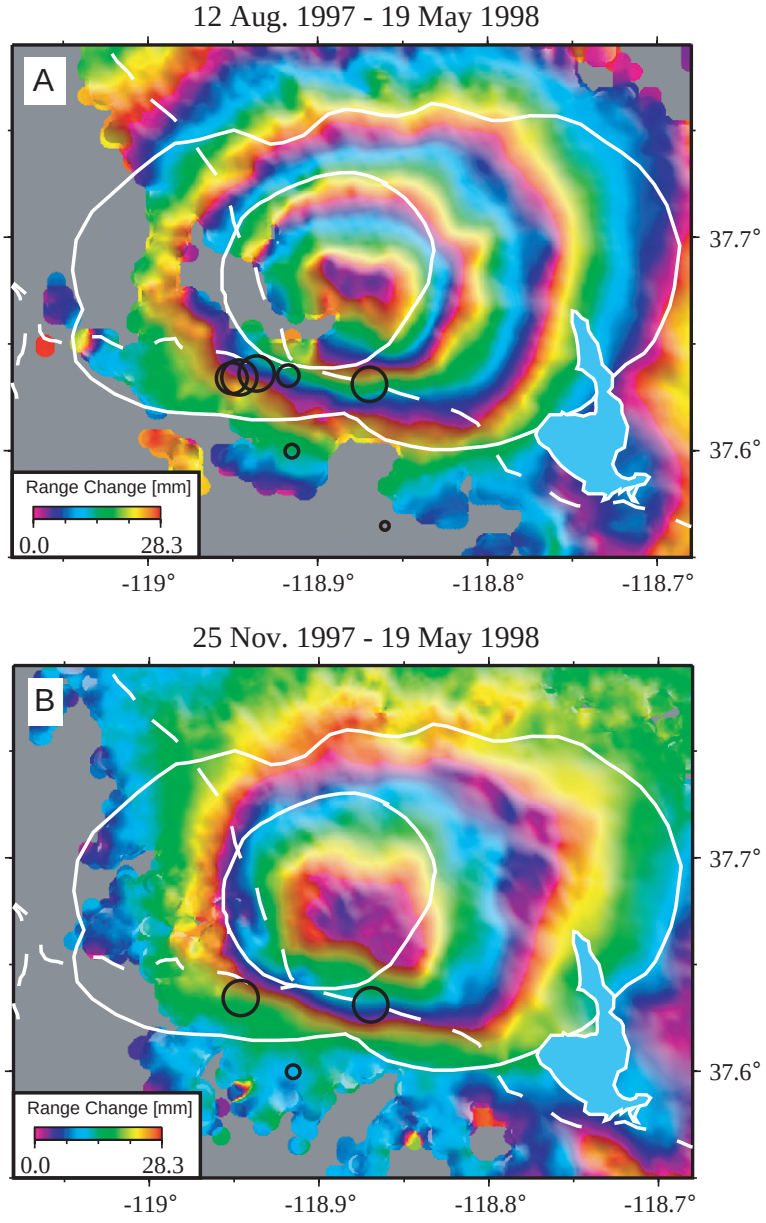

Fig. 4. Interferometric Synthetic Aperture Radar (InSAR) images of Long Valley Caldera created from SAR data pairs (Pair A—12 AUG, 1997 and 19 MAY, 1998; Pair B—25 NOV, 1997 and 19 MAY, 1998) from the ERS-2 descending satellite orbit. Each color "fringe" represents line-of-sight length change (23° off-vertical) across 1/2 wavelength of the radar frequency (28.3 mm for C-band ERS-2 satellite data). Total surface inflation to the center of deformation (bull's eye) is ~10 cm for the period A and ~5 cm for B (a subset of A). Also shown are earthquakes between M_w 4.3 and 4.9 (open circles) occurring in each period. InSAR Data is shown with shaded relief to illustrate the near-vertical aspect of this data.

which shares the same ending scene as A, captures deformation after the onset of major seismic moment release along the South Moat. LOS for these images, which are descending orbits, are 76° CCW from north and 23° from vertical, hence the data mostly reflect vertical deformation, with a small (S14°E) horizontal component. Each color "fringe" represents 28.3 mm of motion in the radar line-of-site, showing a total of approximately 100 mm of inflation at the central "bull's eye". The deformation pattern is radially symmetric with a slight elongation in the east-west direction (same as caldera rim).

Repeat InSAR images from the same orbit measure 1-dimensional displacement, and are spatially continuous, excluding areas of decorrelation, such as occurring within the western portion of the caldera in pairs A and B. However, the combination of these data with GPS and EDM give an essentially complete four-dimensional (three spatial dimensions plus time) image of deformation activity at Long Valley during the 1997–1998 inflation episode.

2.2. Seismic data

Hypocentral earthquake location and magnitude data available from the Northern California Earthquake Data Center (NCEDC, http://quake.geo.berkeley.edu/) are shown for the early 1995 through mid-1997 slow inflation and peak late-1997 inflation (22 November–31 December, 1997), color coded in Fig. 2. The earthquakes are spatially offset from the inflation center, mostly occurring in the South Moat, but are well correlated in time with deformation. The largest earthquakes, 6 $M>4.2$ events (Table 1), followed the exponential increase in inflation (Newman et al., 2001; Hill et al., 2003). Additional, high precision double-differenced relative earthquake locations (Fig. 5) were recorded as part of two temporary arrays installed by the USGS and Duke University (Prejean et al., 2003). Unfortunately, because these data are only available through early September, they miss the major moment release in late November.

These data are useful for assessing the location of the brittle–ductile transition (stresses sufficient for earthquakes cannot build up in ductile material) generally greater than ~300 °C. Additionally, by defining the South Moat Fault (SMF) and movements across it (e.g., Dreger et al., 2000; Langbein, 2003), seismicity helps to explain non-radially symmetric components of observed 1997–1998 deformation.

Table 1
Earthquakes greater than M_w4.2 within Long Valley caldera in late 1997 catalogued by the Northern California Earthquake Data Center (NCEDC)

Date	Latitude	Longitude	Depth	Magnitude NCEDC	[M_w] Dreger
22 Nov 1997	37.6340	−118.9507	8.20	4.7	4.6
22 Nov 1997	37.6352	−118.9175	8.38	4.5	4.6
22 Nov 1997	37.6363	−118.9360	7.66	4.8	4.9
30 Nov 1997	37.6343	−118.9462	7.10	4.8	4.9
29 Dec 1997	37.5998	−118.9153	8.37	4.3	–
31 Dec 1997	37.6312	−118.8697	6.59	4.8	–

Additional moment-inversion based magnitudes are given for events analyzed by Dreger et al. (2000).

3. Models

Volcanic deformation at Long Valley has been assessed by many authors, for spherical, prolate spheroid, ellipsoidal or penny-shaped crack sources with either GPS, EDM, leveling and/or InSAR data (e.g., Langbein et al., 1993, 1995; Tiampo et al., 2000; Newman et al., 2001; Fialko et al., 2001; Battaglia et al., 2003a; Langbein, 2003). With the exception of Newman et al. (2001), who incorporated a VE rheology, models have assumed deformation within a homogeneous, purely elastic medium. Given that Long Valley has had an extensive eruptive history, and is currently undergoing unrest, it is logical to assume that rocks near the inflation source are considerably heated and weakened beyond the brittle–ductile transition temperature where VE rheology is more appropriate. Here we explore a finite element model (FEM) that incorporates a VE shell near the deformation source. We also use a realistic source volume (necessary for assessing source pressures). Because of the potentially large number of variables, the results are non-unique, however they illustrate the impact that viscoelasticity has on time-dependent deformation. Because it is time-intensive to geometrically parameterize and mesh appropriate FEMs, we explore a limited range of geometries derived from source properties determined from prior, published analytical inversions of geodetic data.

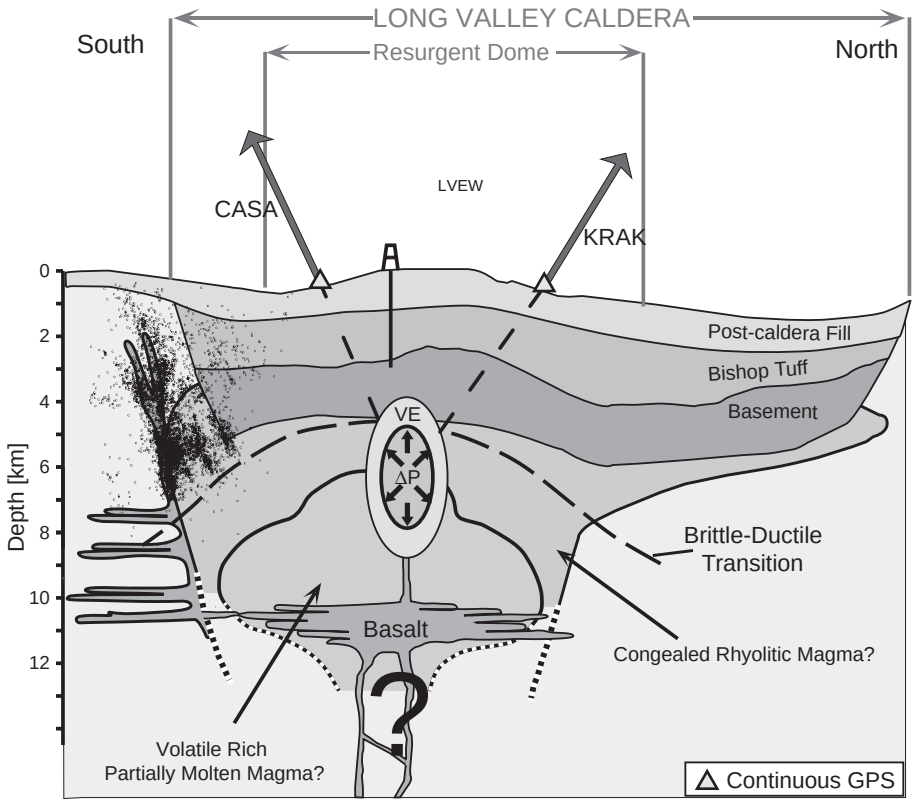

Fig. 5. Schematic cross-section of Long Valley Caldera with no vertical exaggeration (after Hill et al. (1998)), including CASA and KRAK geodetic vectors (arrows) (Newman et al., 2001), high precision South Moat seismicity (small dots) (Prejean et al., 2003), and petrologic interpretations (Bailey, 1989). Also shown is the vertically dipping prolate spheroid pressure source model centered at 6 km with a vertical long half-axis, $a = 1800$ m, and a horizontal short half-axis, $b = 900$ m (central ellipse). The source is surrounded by a 0.5–1 km thick viscoelastic (VE) shell. The location and depth (3 km) of the Long Valley Exploration Well (LVEW) is shown (Fischer et al., 2003). While there is no known link between the volcanic plumbing that drives deformation under the resurgent dome and the faulting and seismicity in the South Moat, the temporal correlation of the two suggests they are closely related.

3.1. Assessing source volume

Geodetic data allows an estimate of volumetric change of the source, ΔV, assuming that deformation occurs within a homogeneous elastic half-space for a given source location and depth. Using the equations of Mogi (1958), McTigue (1987) showed that for a spherical source model, ΔV could be found for either radially horizontal, U_r, or vertical deformation U_z, by:

$$\Delta V = \frac{4\pi}{3} U_r \frac{(d^2 + r^2)^{3/2}}{r}, \Delta V = \frac{4\pi}{3} U_z \frac{(d^2 + r^2)^{3/2}}{d} \quad (1)$$

where r and d are the horizontal and vertical distances between a point of surface deformation and source center. For a prolate spheroid source (an ellipsoid whose two minor axes are of equal length), the analytic equation relating ΔV and U becomes quite complex, but is still controlled solely by the source location and geometry, given a homogeneous purely elastic half-space (Yang et al., 1988; Davis, 1986) (Appendix A).

Assessing source pressure is also important for understanding the physics of volcano deformation and eruption hazard. There is a trade-off between crustal strength and source pressures or volume, thus a lack of understanding of rheology can result in large uncertainty on source volumes and accompanying pressures. In practice, this means that in order to estimate reasonable source pressures, we must assume plausible rheology and source volume. Additionally,

Table 2
Published prolate spheroid source parameters from inversions of geodetic data

Paper	Depth d [km]	Volume change ΔV [km^3]	Axis ratio b/a	Episode [year]
Langbein (2003)[a]	6.0	0.03	0.45[b]	1989
Fialko et al. (2001)	7.2	0.07[c]	0.43	1997–1998
Langbein (2003)[a]	6.0–7.0	0.03	0.85[b]	1997–1998
Battaglia et al. (2003a)	5.9	0.09	0.48[b]	1997–1998
This study	6.0	0.1[d]	0.5	1997–1998

[a] Includes a second deeper source between 10 and 20 km depth.
[b] Converted from stress ratios using Davis (1986).
[c] Volume change is calculated from ΔP=8 MPa and μ=5 GPa (Eq. (2)).
[d] Volume here is assumed for the entire inflationary period between 1978 and 2000.

to place bounds on the total volume involved in expansion it is necessary to assume that since no eruption had occurred, the overall pressure change, ΔP, must remain below the lithostatic load, P_{litho}.

Though aspects of published models for vertically, or near vertically, dipping prolate spheroids at Long Valley vary (Table 2), 1st order approximations of individual parameters are sufficient to test the viscoelastic models in this study. For the 1997–98 episode, depth estimates are between 5.9 and 7.2 km. Langbein et al. (1995) found 5.5 km depth for the 1989 deformation episode. For this study we use an intermediary depth value of 6 km (approximating the average of earlier studies of 6.2 km). The geometric ratio of the semi-minor, b, and semi-major axes, a, b/a=0.43 to 0.85, depending on the data used and model parameters and average 0.55. Here we chose a value slightly more elliptical than the average but closer to 3 of the 4 previous studies, b/a=0.5, which is slightly more spherical than the more pipe-like models with a ratio of 0.45, but much more elliptical than the nearly spherical source, b/a=0.85, found by Langbein (2003) for the 1997–98 source. Because volume change is cumulative, we must assess the uplift between 1978 and 2000 which yields approximately 0.1 km^3 of volumetric increase at the source.

The equation relating ΔV and ΔP for a prolate spheroid within a Poisson's solid is (Tiampo et al., 2000):

$$\Delta P = \frac{\mu \Delta V}{\pi a b^2}. \tag{2}$$

where μ is the rigidity, or shear modulus ($a=b$ for a spherical source). The lithostatic load, P_{litho}, at the top of vertical prolate spheroid pressure source is:

$$P_{\text{litho}} = (d-a)\rho g, \tag{3}$$

where ρ and g are the rock density and local gravitational acceleration. Assuming the maximum allowable pressure within the chamber, $\Delta P_{\max} = P_{\text{litho}}$ (otherwise an eruption occurs) and using an axes ratio b/a=0.5:

$$\Delta P_{\max} = \frac{4\Delta V \mu}{\pi a_{\min}^3} = (d - a_{\min})\rho g. \tag{4}$$

For ΔV=0.1 km^3, d=6 km, ρ=2800 kg/m^3, g=10 m/s^2, and rigidity suitable for hot volcanic region, μ=5 GPa (e.g., Bonafede et al., 1986), we obtain a minimum size for the prolate spheroid, $a_{\min}$=1740 m and $b_{\min}$=870 m. Mathematically, the maximum allowable size goes almost to the surface.

More realistically, the maximum size of the vertically dipping magmatic pressure source at 6 km depth is limited by seismicity and thermal information from the Long Valley Exploration Well (LVEW) (Fischer et al., 2003). Seismicity in the immediate vicinity of the magmatic source region occurs along the South Moat and is mostly above 7 km depth and more than 4 km from the source (Figs. 2 and 5). Given the lack of seismicity directly above the focus of the magmatic center, the source could conceivably be located at very shallow depths. However, local seismic tomography does not image such a body at depths shallower than 3 km (Foulger et al., 2003). Additionally, temperatures at the LVEW site (drilled to 3 km depth approximately 1 km from the magmatic source focus) are only ~100 °C between 2500 and 3000 m depth (Fischer et al., 2003). However, it is evident that the rocks at 2600 m were previously 200 °C hotter, similar to surrounding bore-hole temperatures (Sorey et al., 1991), before changes in the hydrothermal system cooled the local crustal rock (Fischer et al., 2003). The rocks sampled here are currently too cool to be sufficiently ductile to represent the deformation source or its ductile shell. Because of these limitations on the size of the prolate spheroid, we chose a relatively small model source with a=1800 m and b=900 m.

3.2. Viscoelasticity

Material surrounding a long-lived magmatic source should be heated significantly above the

brittle–ductile transition. Above this temperature, rocks no longer behave in a purely elastic manner, but permanently deform because the fluid strength, or viscosity, η, is significantly lowered. However, unless the material contains a significant component of melt, it also maintains a partially recoverable elastic response, and can be modeled as a visco-elastic material (e.g. a Maxwell Fluid). A Maxwell VE fluid, is a linear system, often illustrated as a spring and dash-pot in series. In such a material an imposed stress will cause both an instantaneous, recoverable strain, and a time-dependent, permanent strain, whose rate is controlled by its Maxwell or characteristic time, τ:

$$\tau \approx \frac{\eta}{\mu}. \tag{5}$$

Dragoni and Magnanensi (1989) describe a shell model for volcano deformation, with a spherical pressure source surrounded by a concentric, spherical, Maxwell VE shell within a purely elastic full-space. In the analytical equation's simplest form, that of an instantaneous pressure increase, and a constant rigidity throughout, the radial displacement as a function of radial distance, r_1, and time, t, is:

$$u_{r_1}(r_1,t) = \frac{1}{4}\frac{\Delta P}{\mu}\frac{R_2^3}{r_1^3}\left[1-\left(1-\frac{R_1^3}{R_2^3}\right)e^{-t/\tau}\right], \tag{6}$$

where R_1 and R_2 are the radii from the source center to the source wall and the outer VE shell wall. The characteristic time is

$$\tau = \frac{9}{5}\frac{\eta}{\mu}\left(\frac{R_2}{R_1}\right)^3. \tag{7}$$

Newman et al. (2001) showed that wet rhyolites (containing 5 wt.% H_2O, similar to what is found in Long Valley) near the solidus temperature, ~670 °C, have a viscosity, $\eta \approx 10^{16}$ Pa s. Additionally, for hot quartz-bearing country rock, around 350 °C, η is between 10^{17} and 10^{19} Pa s (Luan and Patterson, 1992; Ivins, 2000). For our model, we use a variable thickness VE shell that is 1 km thick at top and bottom and 0.5 km thick on the sides with a viscosity of 10^{16} Pa s (Fig. 5), to maintain $b/a=0.5$ for the purely elastic half-space outside the VE shell. Davis (1986) first suggested that the ellipsoidal source can include a region of low viscosity rock.

The maximum viscosity that can be investigated depends in part on the time span sampled by a given set of deformation data. Because purely elastic models are time-invariant and often average deformation data over several years, they are not sensitive to possibly low viscosity rheology near the deformation source. Using a prolate spheroid approximation of Eq. (7), we find that depending on the period of the time averaged data, T, the minimum resolvable viscosity, $\eta_{\min}$, can be described as:

$$\eta_{\min} \approx T\mu\left(\frac{a}{a'}\right)\left(\frac{b}{b'}\right)^2 \tag{8}$$

where a' and b' are the radii from the source center to the outer edge of the VE shell in the semi-major and semi-minor directions. Previous prolate spheroid models for Long Valley average data for one to several years, with $T \approx 3$ a, thus will not be sensitive to material with viscosities less than ~10^{17} Pa s (Fig. 6). Alternatively, because our model is time-dependent and compares data measured on a daily basis, our prolate spheroid is potentially sensitive to material with viscosities greater than ~10^{14} Pa s. Thus, for modeling daily sampled time-dependent deformation data it is justifiable to consider a small source surrounded by a VE material with viscosity >10^{14} Pa s. However, for models that average a few years of data, results are insensitive to materials with viscosities below ~10^{17} Pa s.

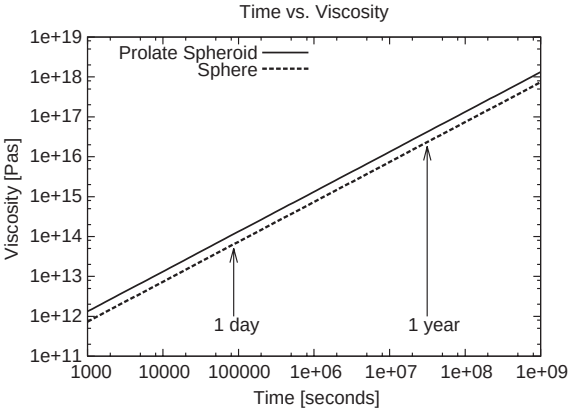

Fig. 6. Sensitivity of temporally averaged data to viscoelasticity surrounding a prolate spheroid or spherical source as describe by Eqs. (7) and (8). Values shown here are for $\mu=5$ GPa, and $a/a'=b/b'=R_1/R_2=0.64$. The apparent difference between the viscosity values for the two source geometries are due to the removal of the constant 5/9 in the prolate spheroid approximation.

3.3. Finite-element magmatic source model

We utilized the finite element method to represent the geometric and temporal complexities of Long Valley deformation due to an inflating source at depth. We used the commercial software package ABAQUS (ABAQUS, Inc., 2003). Our initial approach assumes radial symmetry about the source center, and can be explored with a two dimensional axisymmetric model that is far more efficient than an equivalent full three-dimensional model. Though this model's rheology is more complex than others proposed for Long Valley deformation, it still does not account for the full spatial complexity of deformation sources and rheology as shown in Fig. 5 (a comparison of our model and a more realistic geologic cross-section, modified from Hill et al. (1998)). The source location chosen for this model is 37.687°N, 118.915°W, the approximate location for the 1989 source of Langbein et al. (1995), and other inversion results for the 1997 source (e.g., Fialko et al., 2001; Battaglia et al., 2003a; Langbein, 2003).

The effect of topography can be approximated from Eq. (1), such that the source depth change due to topography, Δd_{topo}, directly above an inflating source will change the predicted vertical deformation by:

$$\Delta U_z = \left(1 - \frac{\Delta d_{\text{topo}}}{d}\right)^2. \quad (9)$$

For the ~400 m elevation increase from the caldera floor to the top of the resurgent dome and areas in the western caldera, the predicted deformation would be ~13% less for a source at 6 km depth. We therefore neglect the effects of topography as its effects are small compared to other uncertainties.

To approximate a half-space, the axisymmetric FEM is composed of ~6100 quadrilateral elements covering a region that extends 50 km horizontally from the source center and 50 km below the surface (Fig. 7). No normal strain is allowed on either side or the bottom (illustrated as "rollers" in Fig. 7). Two elliptical shells within a larger outer spherical shell

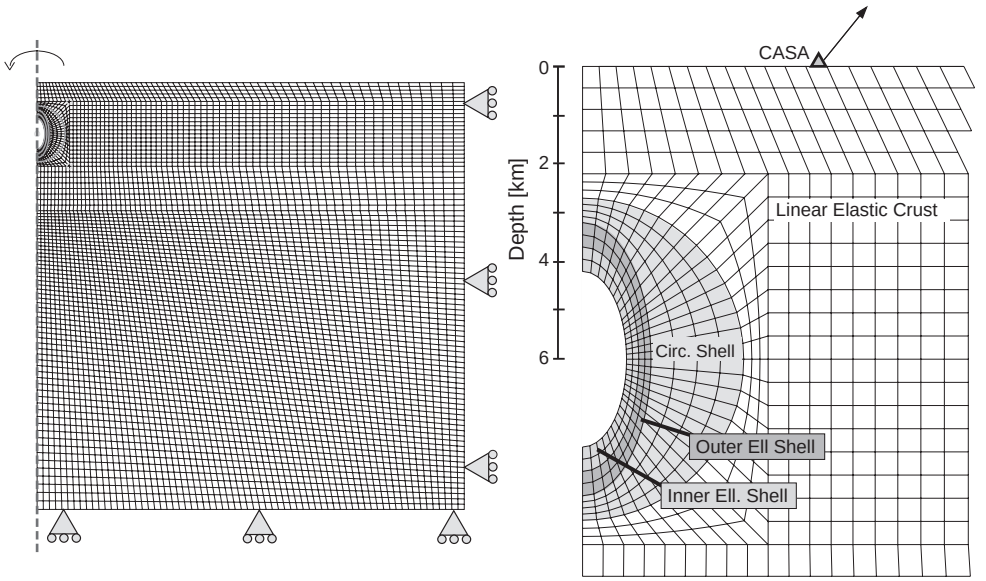

Fig. 7. (Left) The FEM mesh for the axisymmetric model incorporating the vertically dipping prolate spheroid shown in Fig. 5. The 50×50 km^2 model, which approximates a half-space, contains 6100 quadrilateral elements and does not allow for horizontal deformation on the sides nor vertical deformation at the bottom. (Right) Details of the source region in the FEM mesh. Surrounding the source, are three layers of elements whose viscous properties are allowed to change. The inner two layers, the inner and outer ellipsoidal shells, are each 500 m thick at top and base and 250 m thick on the side (variable thickness shells were created to maintain overall spheroid ratio $b/a = 0.5$). The third shell is circular shell with a radius of 3300 m, thus the shell is 500 m thick at top and base and 1400 m on the side. The axis for this model is at 37.687°N, 118.915°W, the source location for the 1989 source of Langbein et al. (1995). For illustration, site CASA is shown with approximate deformation vector, during 1997 episode.

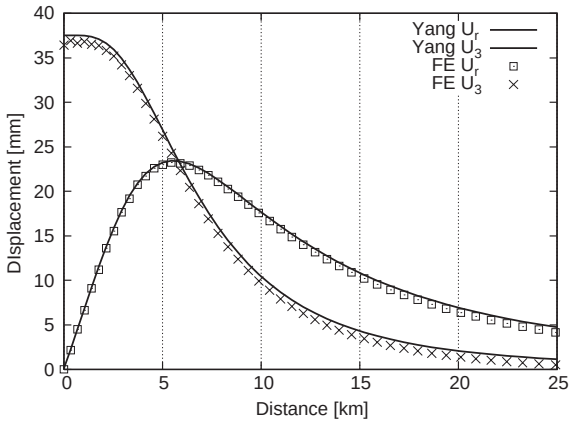

Fig. 8. Comparison of analytic (Yang et al., 1988) and FEM (this study) solutions for deformation. For the model geometry used in this study, the analytic solution is very closely approximated by a purely elastic FEM solution with geometry and mesh shown in Fig. 7. Model parameters are μ, ν, θ, ϕ, P, z_0=5 GPa, 0.25, 90°, 0°, −12.0 MPa, 6 km. To radial distances of 25 km the surface deformation predicted by the FEM closely approximates analytic solution, with average offsets of 0.3 and 0.7 mm in the radial and vertical components. However, the proportional difference becomes significant at distances greater than 10 km (or 20% of the model mesh) where the FEM is about 1/2 the value of the analytic solution and beyond the region of interest in this study.

surround the source center. With this formulation, we can perform some simple numerical experiments to assess the sensitivity of surface deformation data to rheologic complexities at depth.

Newman et al. (2001) found good agreement between a FEM spherical VE shell model surrounding a spherical pressure source, with an analytic equivalent described by Dragoni and Magnanensi (1989). Here we test our FEM approximation of a prolate spheroid in a similar manner. Thus, we compare the FEM, holding μ=5 GPa, and Poisson's ratio, ν=0.25, for all regions outside the source to the Yang et al. (1988) analytic model for the same geometry (θ=90°, P=−12.0 MPa, z_0=6 km; see Appendix). The model geometry and mesh in Fig. 7 were used and ΔP was chosen to approximate the maximum value explored in our models. The FEM solution slightly underestimates the Yang model prediction by 0.3 and 0.7 mm at distances to 25 km (Fig. 8). While this value differs only a few percent in the first 15 km (30% of the lateral extent of the FEM), the offset becomes significant further from the source. This is acceptable because most of the data being compared is within 15 km of the deformation source epicenter. By extending the FEM to 100×100 km^2 (~18,000 quadrilateral elements) the two solutions are nearly identical to 25 km. The smaller model, however, has considerably fewer integrations and is more efficient than the larger model while obtaining good results in the area of interest, and is used for the remainder of this study.

We next introduce the VE component to the inner and outer elliptic shells as described in model VE1 of Table 3. The VE component has the same rigidity as the outer purely elastic components, μ=5 GPa, but has an additional viscous component similar to that of near-solidus wet rhyolite, $\eta=10^{16}$ Pa s, and described in Section 3.2. Using a starting point pressure history, model L-2 from Newman et al. (2001), we performed a series of forward models to best fit the single EDM Baseline between CASA and KRAK (the baseline crossing the central resurgent dome and showing the most deformation). Only the pressure history is varied.

Fig. 9 (bottom) shows the resultant pressure history obtained by fitting the CASA–KRAK EDM baseline

Table 3
Rheologic parameters for several plausible volcanic source models

Model	Inner ellipsoid shell		Outer ellipsoid shell		Circular shell		Linear elastic crust	
	μ	η	μ	η	μ	η	μ	η
VE1	5	1e16	5	1e16	5	∞	5	∞
VE2	5	1e16	5	1e18	5	∞	5	∞
VE3	5	1e16	5	1e16	5	1e18	5	∞
VE4	5	1e16	5	1e16	30	∞	30	∞
LE1	5	∞	5	∞	5	∞	5	∞

All models are variations of the model VE1 (used to fit geodetic data) and maintain the geometry in Fig. 7. Regions with $\eta=\infty$ are purely elastic. Response of these models to the pressure history used to fit VE1 to geodetic data is shown in Fig. 9. Rigidities and viscosities are in GPa and Pa s, respectively.

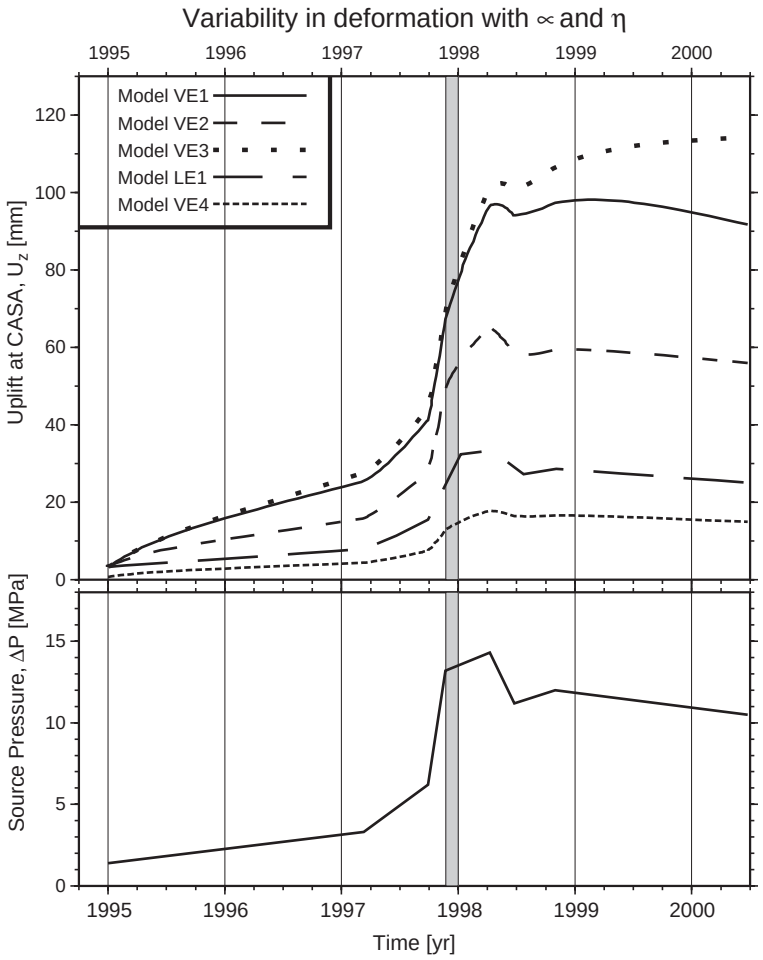

Fig. 9. (Top) Vertical deformation predicted at site CASA for models with varying rheologies while maintaining a constant geometry and pressure history (Bottom). Vertical band represents the period of the six M_w 4.3–4.9 earthquakes (22 November–31 December, 1997) along the South Moat. Note that the peak in seismicity corresponds with a significant decrease in pressure growth rate. All models use the FEM mesh geometry in Fig. 7 and are varied by parameters listed in Table 3. The model VE1 was used to fit geodetic data in Figs. 10 and 11. The predicted vertical deformation varies by nearly an order of magnitude depending on the model.

data while maintaining a minimal number of segments (Table 4). The pressure history consists of seven piece-wise linear and continuous segments, with a maximum ΔP of 14.3 MPa, almost an order of magnitude lower than the lithostatic load near the source top (~115 MPa). The model has a slow and steady increase in pressure between 1995 and early 1997, increasing rapidly through late 1997. On 22 November, 1997 (Day 1056 in Table 4) the pressure increase decelerates rapidly before decaying in early 1998. The onset of this deceleration is coincident with the onset of major seismic moment release across the South Moat, and changes in the GPS and EDM time series. It is likely that the sudden pressure decrease is related to the maximum moment release along the South Moat. This conclusion is consistent with the findings of Newman et al. (2001).

3.4. Effect of rheology on observed deformation

Additional models using the best fit pressure history from model VE1 and varying rigidity and viscosity for individual model components were used to further evaluate rheological effects. Table 3 shows the

Table 4
Pressure history used to for CASA-KRAK EDM baseline for FEM VE1

Time [days]	0	800	1000	1056	1195	1270	1400	2000
ΔP [MPa]	1.4	3.3	6.2	13.2	14.3	11.2	12.0	10.5

Time is in days from January 1, 1995.

rigidity and viscosity values used for individual material sections shown in Fig. 9.

In model VE2, the VE layer was first separated into two layers, the outer being 100× more viscous, analogous to 350 °C granodiorites (country rock) (Luan and Patterson, 1992; Ivins, 2000). Because the model more closely approximates an elastic half-space compared to VE1, with less of a time-dependent character, the modeled vertical deformation at site CASA is 40% smaller and has sharper transitions (Fig. 9).

Model VE3 was used to test the effects of a large spherical shell surrounding the source with a high viscosity ($\eta = 10^{18}$ Pa s), comparable to a region of significantly heated country rock. This model has the same VE shell as VE1. Because this model is similar to VE1, the modeled vertical deformations for site CASA are similar; VE3 predicts about 20% more inflation after the rapid pressure increase in late 1997 compared to model VE1 due to the larger region with higher viscosity.

Model VE4 tests the effects of rigidity on observed deformation. The viscous properties for all materials are the same as in VE1, however the rigidity is increased to typical crustal values of 30 GPa (e.g., Masters and Shearer, 1995), rather than 5 GPa, which has been suggested appropriate for hot volcanic regions (e.g., Bonafede et al., 1986). As expected, because deformation scales inversely with rigidity, the 6-fold increase in rigidity results in about one-sixth the deformation.

Finally, model LE1 was used to show the effects of the pressure history on a purely elastic half-space ($\mu = 5$ GPa). Because there are no time-dependent effects, any change in pressure at the source translates into recoverable instantaneous deformation. The predicted deformation is less than one-third that of VE1 even though the elastic character of each model is the same. Thus, for the given geometry, a purely elastic model requires at least a 3-fold increase in source pressure compared to VE1 to explain the same magnitude of deformation.

4. Discussion

4.1. Agreement of magmatic source model

Chi Square, χ^2, and reduced Chi Square, χ^2_v, results for individual fits are given in Table 5. χ^2 gives the sum of the squared variance between the model, Model_i, and data, Data_i, weighted by individual errors σ_i such that:

$$\chi^2 = \sum_{i=1}^{n} \left(\frac{(\text{Data}_i - \text{Model}_i)}{\sigma_i} \right)^2. \quad (10)$$

Because this value increases with the inclusion of additional data and is not effected by the complexity of the models, by itself, it gives no information about how well can a given model actually approximates data. Thus, it is better to use χ^2_v, as it scales χ^2 by the degrees of freedom (number of data points, N, minus the number of adjustable parameters, M) in a given model fit,

$$\chi^2_v = \chi^2/(N - M). \quad (11)$$

As a model more accurately predicts data, whose errors are correctly assessed, while maintaining a justifiable number of free parameters, this value approaches 1.0 (Press et al., 1992). Thus examining χ^2_v, is a useful assessment of the appropriateness of a given model to explain observed deformation. Though neighboring InSAR pixels are inherently correlated, they are assumed to be independent. Thus, the numerous data we incorporate ($N \approx 34{,}000$; including 14,000 GPS and EDM points and 20,000 InSAR points) and the relatively few free parameters ($M = 16$ for VE volcanic model and 12 for fault models) allows us to assume $N - M \approx N$.

Given the optimal pressure history from the model (VE1), the predicted deformation results were compared to EDM and GPS time-dependent data. Both CASA and KRAK had comparable vertical uplift (between 100–120 mm). This causes the EDM baseline to essentially become a superposition of the hor-

Table 5
Error estimates for fits of geodetic data to volcanic model VE1 and total model, incorporating fault slip (Fig. 13)

Station	Component	Number of points	Volcanic model		Total model	
			χ^2	χ^2_v	χ^2	χ^2_v
GPS						
CASA	Radial	1611	791	0.49	1035	0.64
CASA	Transverse	1611	1922	1.19	3015	1.87
CASA	Vertical	1611	1960	1.22	2144	1.33
KRAK	Radial	828	676	0.82	650	0.78
KRAK	Transverse	828	671	0.81	623	0.75
KRAK	Vertical	828	495	0.60	496	0.59
EDM						
CASA-KRAK	Length	750	1236	1.65	1451	1.94
CASA-SAW	Length	750	29,616	39.49	30,485	40.65
CASA-KNOLLS	Length	709	18,405	25.96	23,706	33.44
CASA-HOT	Length	716	4,405	6.15	6814	9.52
CASA-SHERWIN	Length	764	23,372	30.59	47,480	62.15
CASA-SHARK	Length	761	26,709	35.10	15,272	20.07
CASA-MINER	Length	761	83,519	109.75	96,540	126.86
CASA-TILLA	Length	772	139,923	181.25	85,300	110.49
InSAR						
12/Aug/97-19/May/98*	LOS	9636	7244	0.75	4966	0.51
25/Nov/97-19/May/98*	LOS	10,558	5104	0.48	2858	0.27
	Total:	33,494	346,050	10.33	322,835	9.64

GPS and EDM are evaluated for all data between 1995 and 2000. InSAR data are evaluated at 250 × 250 m patches of pixels within 15 km of the surface expression of the volcanic source in Fig. 11.

izontal components with little sensitivity to vertical deformation. Model VE1 was developed to fit the CASA–KRAK EDM 1-component baseline length change, thus the reduced Chi Square (goodness-of-fit) are relatively low, 1.65. Additionally, good agreement is obtained for the three-component time-dependent data from CASA and KRAK continuous GPS; rotated in radial and transverse components relative to the inflation source (Fig. 10A). If all deformation occurred due to a single radially symmetric source at 37.687°N, 118.915°W with no residual component of NAP or SNB motion, then the transverse component, U_T, on each GPS receiver is expected to be zero. The very small U_T of KRAK suggests little off-axis deformation, and is coincident with the earthquake activity along the SMF. This is an unexpected result since CASA is in closer proximity to the SMF yet lacks a similar offset. This effect is likely related to the fact that the direction of South Moat motion at site CASA was coincident with the direction of the radial component and has only a minor effect on the transverse component. It is arguable that the offsets observed here are not statistically significant, as evidenced by the small χ^2_v values for the transverse components of GPS. Offsets are more robust in several of the EDM data and are not explained by the volcanic source model (Fig. 10B).

The predicted time-dependent deformation from VE1 is shown along with data for the 8 frequently observed EDM reflectors from CASA in Fig. 10B. The fit of the CASA–KRAK baseline is explicitly small ($\chi^2_v = 1.65$) since this baseline was used to define the source pressure history. The baselines for the four reflectors north of CASA and crossing the resurgent dome all do reasonably well, with the best fit for the CASA–HOT baseline (~80 °CW from KRAK), however the model overpredicts deformation for both the SAW and KNOLLS baselines. This is possibly due to a combination of unmodeled effects of hydrothermal pumping at Casa Diablo, and more likely the failure of the axisymmetric model to assess possible lateral variations in crustal strength (discussed later). Simply enough, a 50% increase in rigidity (from 6 to 3× lower than cool continental crust) in regions west of the central resurgent dome would cause a reduction in surface

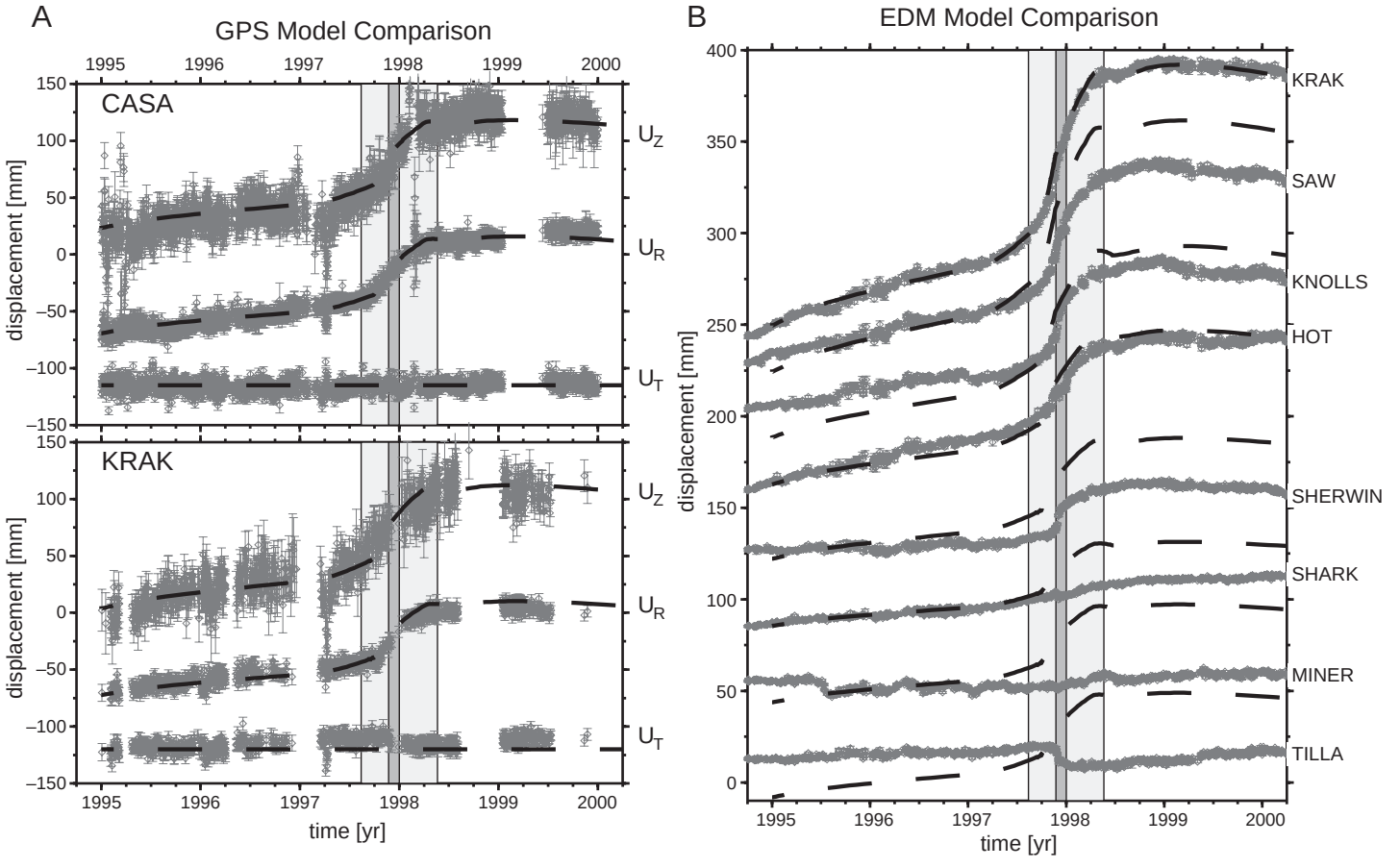

Fig. 10. Observed and predicted (A) GPS and (B) EDM deformation using model VE1 and the pressure history in Table 4: Vertical, radial and transverse components of measured and predicted (dashed line) displacements are shown at continuous GPS sites CASA and KRAK shown on Fig. 2. Baseline length changes between the base station, CASA, and individual reflector stations, shown in Fig. 4. Gray period shows the time covered by the InSAR image pair and model results in Fig. 11. EDM stations CASA and KRAK correspond to GPS stations with the same name. EDM baselines shot across the resurgent dome (top four) closely fit model prediction (dashed lines). However, sites measured across the south of the resurgent dome (bottom four) and around the seismically active South Moat, poorly match model prediction. Offsets in deformation on tangential component of GPS site KRAK and on the CASA–TILLA EDM baseline correspond to peak in South Moat seismicity.

deformation, similar to what is seen here. Each of the four predicted southern baselines, which either near or cross the seismically active SMF, poorly match the data resulting in high χ_v^2 values. In the case of TILLA, the data go the opposite direction, during the peak in South Moat seismicity. We initi-

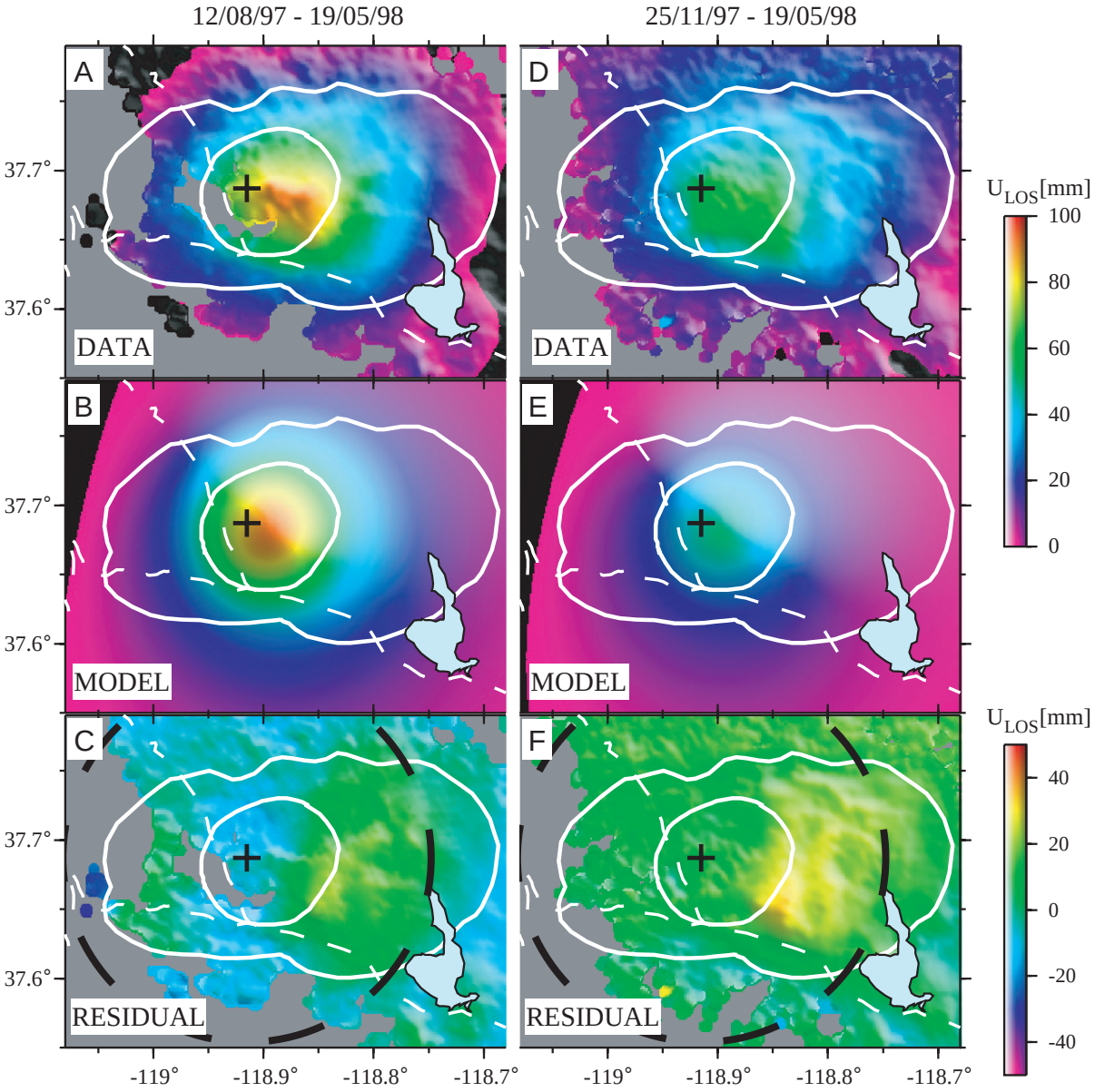

Fig. 11. InSAR pairs shown in Fig. 4, "unwrapped" and converted to LOS displacement (A, D). Small cross within the resurgent dome designates the center of deformation in volcanic source model, VE1. Modeled deformation in InSAR LOS for the same periods is shown (B, E). Because ERS SAR imagery is 20° east of vertical, data and modeled inflation are offset from the source epicenter. The resulting residuals are generally low, but underpredict measured data in the south east and near the eastern extent of the South Moat (C, F). Dashed circles enclose the region used to calculate χ^2 misfit (15-km radius).

ally interpret this misfit to be related to fault-related deformation, and will further discuss it in the following section.

Model results were then compared to InSAR data in Fig. 4, spanning most of the 1997–98 inflation episode, to understand the applicability of model VE1 to the spatial extent of deformation within the caldera. Fig. 11 shows the same InSAR images from Fig. 4, unwrapped and converted to displacement (A and D). Also shown are the VE1 modeled LOS deformation for the duration of the InSAR pairs (B and E) and residuals (C and F). The modeled peak inflation is offset from the source axis (+ in Fig. 11), because LOS is about 20 °E of vertical. Overall, model VE1 closely approximates InSAR data, with low χ_v^2 values, particularly for InSAR pair-B, where $\chi_v^2 = 0.48$. Generally the volcanic model underpredicts the data in the southeast for either model, and near the eastern portion of the SMF. Though low χ_v^2 values for both InSAR pairs suggest the time-dependent volcanic model, VE1, accurately describes all deformation within error, poor fits to EDM data across four southern baselines and overall underprediction of InSAR data near the SMF suggests that fault slip associated with seismic activity is responsible for much of the remaining deformation.

4.2. Fault slip models

EDM and InSAR data have components of unmodeled deformation that are spatially and temporally correlated with the six M 4.3–4.9 right-lateral, strike-slip earthquakes along the SMF in late-November 1997 (Table 1). These individual events correspond to apparent offsets in the GPS and more notably EDM data on 22 Nov., 30 Nov., and 31 Dec. 1997 (Fig. 12).

In order to assess the data offsets we start with the distributed fault models 9a and 9b from Langbein (2003). These values were obtained from a joint inversion for magmatic inflation and SMF slip, within a purely elastic half-space to describe the cumulative 1997–1998 deformation as measured by available EDM data. Because this study assesses the time-dependent nature of deformation, incorporates additional geodetic data-types, and includes a modestly different volcanic source, we chose to modify Langbein's slip model. We chose to minimize the offset of EDM data across the four southern baselines in late

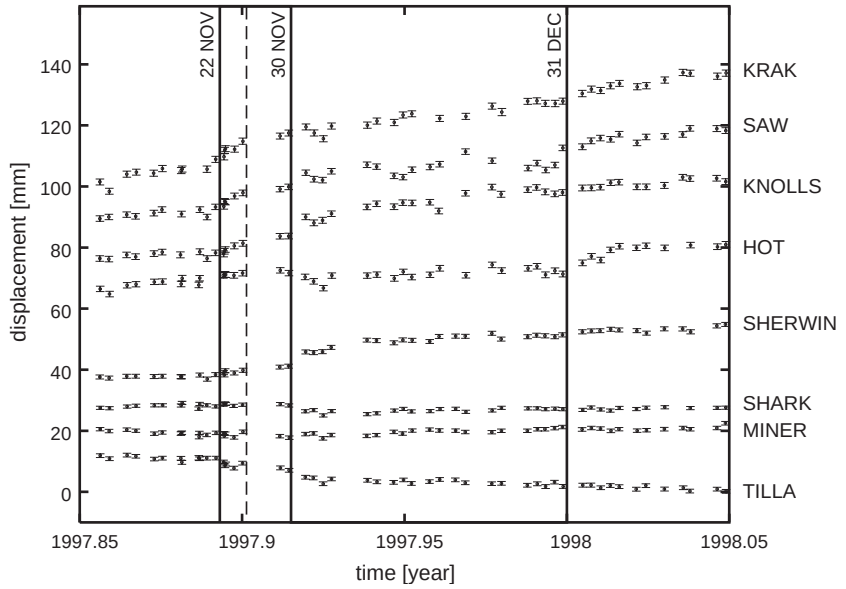

Fig. 12. Close-up of EDM measurements during M_w 4.3–4.9 earthquakes in late 1997. Small offsets are visible after three M_w 4.6–4.9 earthquakes on 22 Nov. and a M_w 4.8 earthquake on 30 Nov. in the western South Moat near the SHERWIN reflector. On 31 Dec. another M_w 4.8 earthquake occurred on the eastern portion of the South Moat near the TILLA reflector. Event hypocenters and magnitudes are listed in Table 1.

Table 6
All faults are right-lateral strike–slip, dipping northward at 70° and striking N80°W

Name	Slip [m]	Length [km]	Depth [km]	Width [km]	Longitude	Latitude
TILLA1	0.40	3.00	3.00	1.00	−118.8805	37.6161
SHERWIN1	0.10	2.00	4.00	1.00	−118.9400	37.6247
SMF1	0.20	10.00	3.50	2.00	−118.9103	37.6204

Latitude, longitude and depth are the surface projection and depth to the center of the fault top. Length and width describes the horizontal and down-dip dimensions from the fault top.

1997, while maintaining the overall character of the Langbein model, by requiring all slip to occur on the SMF and having two centers of maximum slip centered near reflector sites SHERWIN and TILLA, and near major seismic moment release. Similar to Langbein (2003), we did not address proposed dilitation across the SMF Dreger et al. (2000), because no abrupt lengthening was observed in EDM baselines SHARK and MINER after the 22 Nov. and 30 Nov. earthquakes (Fig. 12). This suggests that if coseismic opening did occur along the SMF, it was transient and closed before the next EDM measurements, or was highly localized and did not effect much of the measured data.

To determine surface displacement we used the analytic solutions due to finite slip from Mansinha and Smylie (1971). Our best fitting solution incorporates three faults (TILLA1, SHERWIN1 and SMF1) corresponding to right-lateral strike-slip, on a single SMF, dipping northward at 70° and striking N80°W (Table 6, Fig. 13). Slip from faults TILLA1 and

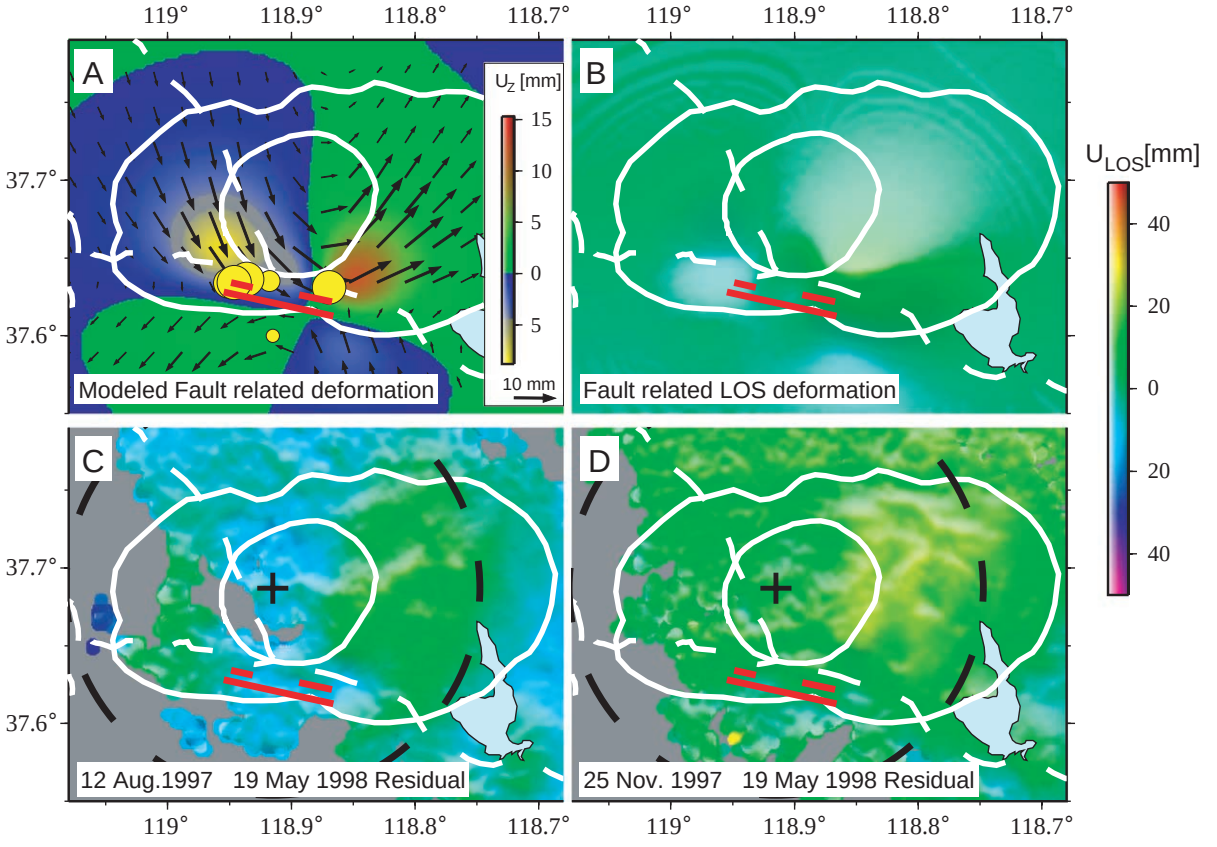

Fig. 13. Modeled displacement due to slip along the South Moat. (A) Predicted horizontal (arrows) and vertical deformation (color map) are due to a series of slips along the South Moat Fault (SMF) listed in Table 6 (red lines; smaller slips are offset to the north for illustration). (B) Model results are converted to InSAR LOS, and subtracted from InSAR residuals in Fig. 11 to get the total residuals (C, D). Dashed circles enclose the region used to calculate χ^2 misfit (15-km radius).

SHERWIN1 occur on a portion of SMF1, essentially creating one slip, with two areas of strain localization, similar to Langbein's (2003) model 9b. Though the overall slip areas are similar, the total geodetic moment release modeled here is moderately smaller, 1.6×10^{17} Nm rather than 2 to 3×10^{17} Nm, and closer to the approximated seismic moment release of all earthquakes for this time ~1×10^{17} Nm for this period (Newman et al., 2001).

We convert the predicted horizontal and vertical surface deformation from the fault models to InSAR LOS displacement (Fig. 13. A, B). We then remove the predicted LOS displacement from the volcanic residuals for InSAR pairs A and B in Fig. 11 to obtain the residual deformation for the total model, including both volcanic and fault-related deformation (Fig. 13. C, D). The results show that including the fault model moderately improves the fit to InSAR data, lowering the χ^2_v values for both pairs from 1.23 and 0.49 for just the volcanic model to 0.99 and 0.28 for the total model (Table 5). Though the second InSAR pair begins after 3 of the 6 large earthquakes on the SMF, the fault model allows for similar improvements in fit. This suggests that most of the modeled geodetic moment release occurs between 25 Nov. 1997 and 19 May 1998. The three earthquakes before 25 Nov. represent only a modest seismic moment release, $M_0=4\times10^{16}$ Nm, one quarter of the total modeled geodetic moment release assuming crustal values of rigidity.

The fault model creates mostly sub-centimeter deformations across the individual GPS components and EDM baselines (Table 7). The fault deformation is accommodated as a shift in all GPS and EDM data on 25 Nov. 1997 and is shown in Fig. 14. For GPS and northern EDM baselines the effect of the predicted fault-related deformation is minimal. For the southern EDM sites DC-offsets are largely removed, particularly for sites SHERWIN and TILLA. However, this inclusion of the faults improved statistical fits for EDM data by less than 5%, with most EDM baselines having worse fits, but modestly improving the poor fit to TILLA. Including the fault model slightly affects the GPS fits with improved fits at KRAK and worse fits for CASA. Because we evaluate simple volcanic and fault models with relatively few adjustable parameters compared to the number of data the problem is extremely overdetermined. Thus the inclusion of additional parameters come at little cost and offer a real improvement as long as they reduce the overall χ^2_v value. Such is the case here where the addition of the fault model reduces the overall value from 9.05 to 8.43.

Table 7
Predicted deformation from faults in Table 6

Name	East [mm]	North [mm]	Vertical [mm]	Baseline [mm]
GPS				
CASA	10.9	−4.5	−3.9	–
KRAK	2.8	−0.4	0.1	–
EDM				
CASA-KRAK	–	–	–	2.6
CASA-SAW	–	–	–	0.4
CASA-KNOLLS	–	–	–	3.2
CASA-HOT	–	–	–	3.0
CASA-SHERWIN	–	–	–	8.9
CASA-SHARK	–	–	–	−4.7
CASA-MINER	–	–	–	2.7
CASA-TILLA	–	–	–	−10.3

For EDM baselines that extend near or cross to the south of the SMF, models consistently overpredict deformation (Fig. 10B). Additionally, with the exception of a small offset on MINER in 1995, the four EDM baselines are linear and nearly flat until the large seismic moment release in late 1997, after which only, SHERWIN begins deforming similarly, but less than the model prediction. InSAR data does not appear to be similarly deficient in deformation in the southern region. At distances greater than 6 km, which includes the region south of the SMF, deformation from the modeled source is mostly horizontal (Fig. 8), thus the EDM data, which are most sensitive to horizontal deformation, would be more affected by volcanic deformation here than InSAR, which is mostly vertical. Overall, it appears that the SMF acts as a barrier that reduces volcanic deformation south of it. The cause for this is unknown, but could be due to increased crustal strength in cooler rock away from the volcanic source or from frictional decoupling along the SMF.

In comparing deformations from models VE1 and VE4, with $\mu=5$ and 30 GPa corresponding to hot volcanic and normal cool continental crust, we note that deformation scales inversely with rigidity, such that for harder crust we expect about 1/6th the deformation seen in volcanic regions. Southern EDM sites

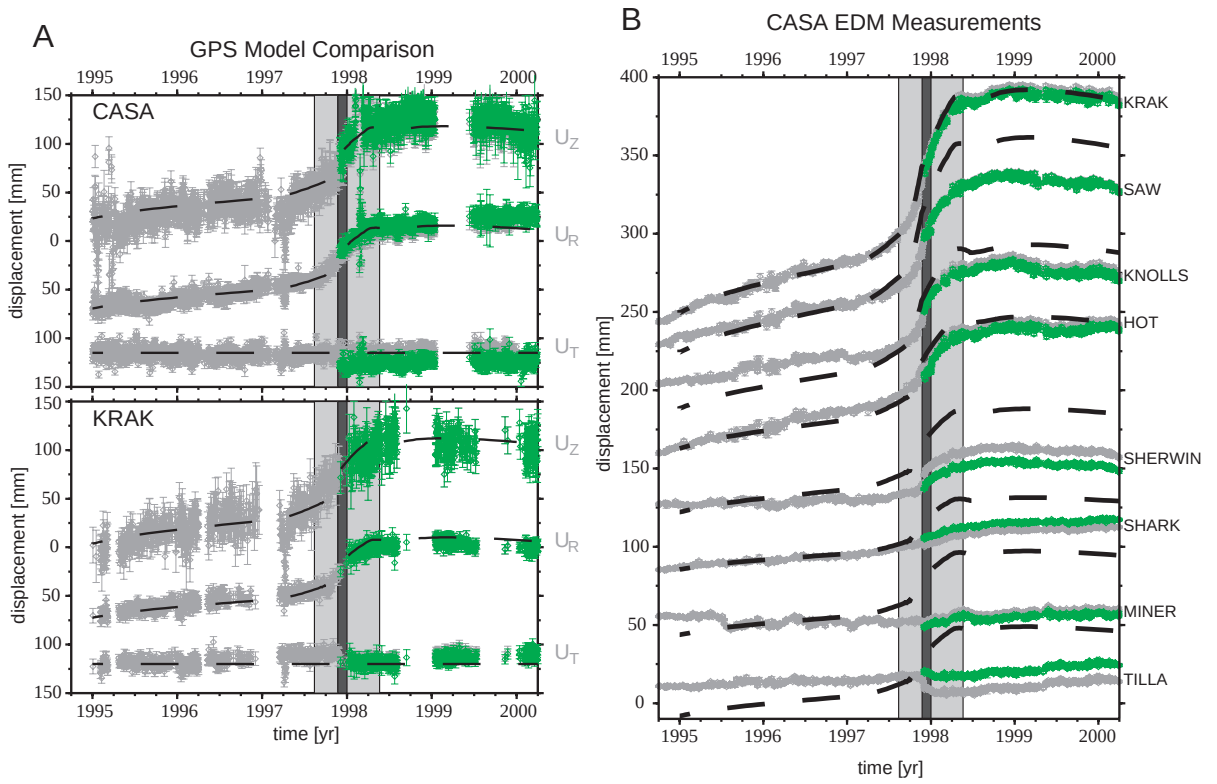

Fig. 14. (A) GPS and (B) EDM data (gray points) and modeled volcanic deformation (dashed black lines) shown in Fig. 10 with offsets due to modeled slip (Fig. 13, Table 7) along the South Moat removed (green). Offsets are small and generally within daily position errors for both the GPS data and EDM data for the 4 north sites, however, offsets become significant across the south, where sites come near or cross the fault. After correcting for fault slip, data at sites MINER, TILLA and SHARK are generally linear, suggesting they record little time dependent deformation due to the volcanic inflation source.

TILLA and MINER lack the 1–2 km caldera fill Bishop's Tuff that underlies the rest of the EDM and GPS data, but are directly over Cretaceous granodiorites and Paleozoic metamorphic rock with abnormally high rigidity near 50 GPa (Bailey, 1989; Charco et al., 2004), further reducing the surface deformation. This effect would not be easily resolvable in the InSAR data due to the near horizontal signal expected from the predominant volcanic source, however would appear on the essentially horizontal EDM data. Thus, the lack of observed deformation at EDM baselines more distal to the volcanic source may be significantly effected by a similar change in rigidity due to thermal and/or compositional changes.

The onset of large $M>4.2$ earthquakes in late 1997, which constitutes the largest seismic moment release since 1983, is coincident with the onset of modeled source pressure deceleration, $dP/dt^2<0$, in model (Fig. 9). However, for all periods within volcanic model VE1, the pressure source consistently creates a small positive normal force on the SMF, $\sigma_{33}=0.05$–0.25 MPa. This force is not large enough, and of the wrong orientation to be directly responsible for the largely dilitational activity observed in some of these events (Dreger et al., 2000; Foulger et al., 2004). Thus, if the SMF did open during these earthquakes, it may be that there is an additional inflationary source, possibly an E–W striking dike (e.g. Savage and Cockerham, 1984; Savage et al., 1987; Langbein et al., 1995) or hydrolic fracturing (Foulger et al., 2004), beneath the SMF. The presence of possible hydrothermal or magmatic material in the SMF may cause frictional decoupling and, at least partially be responsible for lower than expected deformation from the volcanic source in the region south of the SMF.

5. Conclusions

A single radially symmetric prolate spheroid pressure source within a thin 0.5 to 1 km VE shell with a relatively simple and small magnitude pressure history, can explain the majority of the observed four dimensional time-dependent geodetic data, temporally continuous GPS and EDM and spatially continuous InSAR, over the period of 1995 to 2000, including the 1997–98 inflation episode at Long Valley caldera. The geometry of the vertically dipping prolate spheroid (twice as tall as wide at 37.687°N, 118.915°W and 6 km depth) and the viscosity and thickness of the surrounding layers are constrained by previous studies. However, the source volume, was shown here to require the long-term pressure increase (between 1978 and 2000) to be less than the lithostatic load, as well as agree with observed seismic and deep borehole data. In this study we present the first geodetically constrained magmatic source volume responsible for deformation at Long Valley, a critically important value for assessing the internal pressures that cause deformation and possible future eruptions. This volume can include semi-solid crustal or partially molten magma with viscosities lower than $\eta = 10^{14}$ Pa s. For the time period studied, the VE model required only a modest pressure increase of about 14 MPa, far lower than the lithostatic load, about 115 MPa. The pressure grew slowly between 1995 and early 1997 before rapidly accelerating until 22 November 1997, the onset of major seismic moment release along the South Moat. At that point, the pressure continued to grow but at a considerably lower rate before decaying in early 1998. For a purely elastic model with the same geometry and rigidity, the maximum pressure change necessary to describe the 1995 through 2000 inflation is around 40 MPa, thus the inclusion of a VE component significantly lowers the necessary pressures.

Combining deformation due to slip along the SMF with VE volcanic deformation allows for a modest improvement to data examined. However, the sum of the models still do not fully explain increased deformation in the eastern part of the caldera or lower than expected deformation south of the SMF. These anomalies may be due to additional unmodeled fault slip, unmodeled inflationary sources, changes in lateral crustal strength and/or the effects of frictional decoupling along the SMF. Though the model described here is certainly non-unique, it provides a considerable advance over purely elastic models in defining the time-dependent nature and the pressures necessary to create the observed deformation at Long Valley Caldera. This is because the inclusion of significant viscoelastic material and reduced crustal strength near a magmatic source, which is geologically expected, considerably reduces the pressure necessary to create observed surface deformation.

Acknowledgments

We thank D. Coblentz, J. Dixon, J. Langbein and G. Mattioli for critical reviews of this manuscript and for many useful suggestions to better this paper. We thank P. Lundgren, Y. Fialko and P. Davis for the corrections to the Yang et al. (1988) analytic model in the Appendix. We thank S. Larson for his 'disl' computer implementation of Mansinha and Smylie (1971). We thank J. Langbein at the United States Geological Survey who provided the EDM data. We used the Generic Mapping Tools (GMT) to create most figures in this manuscript (Wessel and Smith, 1998). Interferometric processing was performed using the JPL/Caltech repeat orbit interferometry package, ROI_PAC, version 2.1. The work was funded by Los Alamos National Laboratory Postdoctoral Fellowship to AVN and NASA and ONR grants to THD (CSTARS publication 3). The manuscript is approved for unlimited public release by the Los Alamos National Laboratory; LA-UR-04-4204.

Appendix A. Corrections to Yang et al. (1988)

This appendix defines corrections to the analytic model for surface deformation from a dipping prolate spheroidal pressure source in an elastic half-space (Yang et al., 1988). These corrections come from computer code modified by John Langbein, Yuri Fialko and Paul Davis. With the exception of the corrections noted here, Yang et al. (1988) appears to be correct for a vertically dipping prolate spheroid since the analytic solutions match finite-element models for the same parameters (Fig. 8). The full analytic derivation, however, was not tested here because we

only compared analytic results to FEM solutions for vertically dipping prolate spheroids ($\theta=90^\circ$). Because of a singularity in the analytic solution at $\theta=90^\circ$, comparisons were done at $\theta=89.99^\circ$.

$$a_{11} = 2R(I_a - 4\pi) \quad (A-1)$$

$$a_{12} = -2R(I_a + 4\pi) \quad (A-2)$$

$$a_{21} = Qa^2 I_{aa} + RI_a - 1 \quad (A-3)$$

$$a_{22} = -\left(Qa^2 I_{aa} + I_a(2R - Q)\right) \quad (A-4)$$

$$P^{\updownarrow}\frac{2\mu P}{3\lambda + 2\mu}\frac{(3a_{22} - a_{12}) - (a_{11} - 3a_{21})}{(a_{11}a_{22} - a_{12}a_{21})} \quad (A-5)$$

$$P^{*} = \frac{P}{3\lambda + 2\mu}\frac{(3a_{22} - a_{12})\lambda + 2(\lambda + \mu)(a_{11} - 3a_{21})}{(a_{11}a_{22} - a_{12}a_{21})} \quad (A-6)$$

$$\bar{y}_3 = \bar{x}_3 + \bar{\xi}_3 \quad (A-7)$$

The following corrections are included but were not tested because they are onlyused when $\theta<90^\circ$.

$$F_1^{*} = 2z\left\{q_2\cos\theta\left[\frac{2a_1}{R_2^3(R_2 + \bar{q}_3)} - \cdots\right] + \cdots\right\} \quad (A-8)$$

$$f_2 = \cdots\left[\cdots + \cos\theta\left(R_2 - \bar{y}_3\right)\right] - 2\bar{A}_2\cos\theta + \cdots \quad (A-9)$$

References

ABAQUS, Inc., 2003. Abaqus User's Manual, Version 6.4. Tech. Rep. Hibbit, Karlsson and Sorenson, Inc., Pawtucket, Rhode Island.

Bailey, R.A., 1989. Geologic map of the Long Valley caldera, Mono–Inyo Craters volcanic chain, and vicinity, eastern California. Map I-1933, USGS Misc. Invest. Series, U.S. Government Printing Office.

Bailey, R.A., Dalrymple, G.B., Lanphere, M.A., 1976. Volcanism, structure and geochronology of Long Valley caldera, Mono County, California. J. Geophys. Res. 81, 725–744.

Battaglia, M., Roberts, C., Segall, P., 1999. Magma intrusion beneath Long Valley caldera confirmed by temporal changes in gravity. Science 285, 2119–2122.

Battaglia, M., Segall, P., Murray, J., Cervelli, P., Langbein, J., 2003a. The mechanics of unrest at Long Valley caldera, California: 1. Modeling the geometry of the source using GPS, leveling and two-color EDM data. J. Volcanol. Geotherm. Res. 127, 195–217.

Battaglia, M., Segall, P., Roberts, C., 2003b. The mechanics of unrest at Long Valley caldera, California: 2. Constraining the nature of the source using geodetic and micro-gravity data. J. Volcanol. Geotherm. Res. 127, 219–245.

Bonafede, M., Dragoni, M., Quareni, F., 1986. Displacement and stress fields produced by a centre of dilation and by a pressure source in a viscoelastic half-space: application to the study of ground deformation and seismic activity at Campi Flegrei, Italy. Geophys. J. R. Astron. Soc. 87, 455–485.

Charco, M., Fernndez, J., Tiampo, K., Battaglia, M., Kellogg, L., McClain, J., Rundle, J.B., 2004. Study of volcanic sources at Long Valley caldera, California, using gravity data and a genetic algorithm inversion technique. Phys. Earth Planet. Inter. 161 (7), 1399–1413, doi: 10.1007/s00024-004-2511-8.

Davis, P.M., 1986. Surface deformation due to inflation of an arbitrarily oriented triaxial ellipsoidal cavity in an elastic half-space, with reference to Kilauea volcano, Hawaii. J. Geophys. Res. 80, 4094–4102.

Dixon, T.H., Bursik, S., Kornreich-Wolf, M., Webb, F., Farina, F., Rubaudo, S., 1993. Constraints on deformation of the resurgent done, Long Valley Caldera, California from Space Geodesy. In: Smith, D.E., Turcotte, D.L. (Eds.), Geodynamics Series: Contributions of Space Geodesy to Geodynamics: Technology, vol. 23. AGU, Washington D.C., pp. 193–214.

Dixon, T.H., Farina, F., Mau, A., Webb, F., Bursik, M., Stein, R., Marshall, G., 1995. GPS monitoring data for active volcanos available on the Internet. Trans. Am. Geophys. Union (EOS) 76, 2.

Dixon, T.H., Mao, A., Bursik, M., Heflin, M., Langbein, J., Stein, R., Webb, F., 1997. Continuous monitoring of surface deformation at Long Valley Caldera, California, with GPS. J. Geophys. Res. 102, 12017–12034.

Dixon, T.H., Miller, M., Farina, F., Wang, H., Johnson, D., 2000. Present-day motion of the Sierra Nevada block and some tectonic implications for the Basin and Range province, North American Cordillera. Tectonics 19, 1–24.

Dragoni, M., Magnanensi, C., 1989. Displacement and stress produced by a pressurized, spherical magma chamber, surrounded by a viscoelastic shell. Phys. Earth Planet. Inter. 56, 316–328.

Dreger, D.S., Tkalcic, H., Johnston, M., 2000. Dilational processes accompanying earthquakes in the Long Valley Caldera. Science 288, 122–125.

Dvorak, J.J., Dzurisin, D., 1997. Volcano geodesy: the search for magma reservoirs and the formation of eruptive vents. Rev. Geophys. 35, 343–384.

Fialko, Y., Simons, M., Khazan, Y., 2001. Finite source modelling of magmatic unrest in Socorro, New Mexico, and Long Valley, California. Geophys. J. Int. 146, 191–200.

Fink, J.H., 1985. The geometry of silicic dikes beneath the Inyo Domes. J. Geophys. Res. 90, 11127–11134.

Fischer, M., Röller, K., Küster, M., Stöckhert, B., McConnell, V.S., 2003. Open fissure mineralization at 2600 m depth in Long Valley Exploratory Well (California)—insight into the history of

the hydrothermal system. J. Volcanol. Geotherm. Res. 127, 347–363.
Foulger, G.R., Julian, B.R., Pitt, A.M., Hill, D.P., Malin, P.E., Shalev, E., 2003. Three-dimensional crustal structure of Long Valley caldera, California, and evidence for the migration of CO_2 under Mammoth Mountain. J. Geophys. Res. 108 (B 3, 2147), doi: 10.1029/2003GL018334 (ESE 6, 1-16).
Foulger, G.R., Julian, B.R., Hill, D.P., Pitt, A.M., Malin, P.E., Shalev, E., 2004. Non-double-couple microearthquakes at Long Valley caldera, California, provide evidence for hydraulic fracturing. J. Volcanol. Geotherm. Res. 132, 45–71.
Hill, D.P., Johnston, M.J.S., Langbein, J.O., McNutt, S.R., Miller, C.D., Mortensen, C.E., Pitt, A., Rojstaczer, S., 1991. Response plans for volcanic hazards in the Long Valley caldera and Mono Craters area, California. U.S. Geol. Surv. Open-File Report, vol. 91-270. U.S. Government Printing Office.
Hill, D.P., Sorey, M.L., Ellsworth, W.L., 1998. Scientific drilling continues in Long Valley caldera, California. Trans. Am. Geophys. Union (EOS) 79, 429.
Hill, D.P., Langbein, J.O., Prejean, S., 2003. Relations between seismicity and deformation during unrest in Long Valley caldera, California, from 1995 through 1999. J. Volcanol. Geotherm. Res. 127, 175–193.
Ivins, E.R., 2000. Correction to "Transient creep of a composite lower crust: 2. A polymineralic basis for rapidly evolving post-seismic deformation modes". J. Geophys. Res. 105, 3229–3232.
Langbein, J.O., 1989. Deformation of the Long Valley caldera, eastern California, from mid-1983 to mid-1988: measurements using a two color geodimeter. J. Geophys. Res. 94, 3833–3849.
Langbein, J.O., 2003. Deformation of the Long Valley caldera, California: inferences from measurements from 1988 to 2001. J. Volcanol. Geotherm. Res. 127, 247–267.
Langbein, J., Johnson, H., 1997. Correlated errors in geodetic time series: implication for time-dependent deformation. J. Geophys. Res. 102, 591–604.
Langbein, J.O., Hill, D.P., Parker, T.N., Wilkinson, S.K., 1993. An episode of re-inflation of the Long Valley caldera, eastern California, 1989–1991. J. Geophys. Res. 98, 15851–15870.
Langbein, J.O., Dzurisin, D., Marshall, G., Stein, R., Rundle, J., 1995. Shallow and peripheral volcanic sources of inflation revealed by modeling two-color geodimeter and leveling data from Long Valley caldera, California, 1988–1992. J. Geophys. Res. 100, 12487–12495.
Luan, F.C., Patterson, M.S., 1992. Preparation and deformation of synthetic aggregates of quartz. J. Geophys. Res. 97, 301–320.
Mansinha, L., Smylie, D.E., 1971. The displacement fields of inclined faults. Bull. Seismol. Soc. Am. 61, 1433–1440.
Mao, A., Harrison, C., Dixon, T., 1999. Noise in GPS time series. J. Geophys. Res. 104, 2797–2816.
Masters, T.G., Shearer, P.M., 1995. Seismic models of the earth: elastic and anelastic. In: Ahrens, T.J. (Ed.), Global Earth Physics: A Handbook of Physical Constants, AGU Reference Shelf, vol. 1. American Geophysical Union, Washington, DC, pp. 88–103.
McTigue, D.F., 1987. Elastic stress and deformation near a finite spherical magma body: resolution of the point source paradox. J. Geophys. Res. 92, 12931–12940.
Miller, C.D., 1985. Holocene eruptions at the Inyo volcanic chain, California: implications for possible eruptions in Long Valley caldera. Geology 13, 14–17.
Mogi, K., 1958. Relations between the eruptions of various volcanoes and the deformations of the ground surfaces around them. Bull. Earthq. Res. Inst. 36, 99–134.
Moran, S.C., Kwoun, O., Masterlark, T., Lu, Z., 2005. On the absence of InSAR-detected volcano deformation spanning the 1995–1996 and 1999 eruptions on Shishaldin volcano, Alaska. J. Volcanol. Geotherm. Res. 150, 119–131. doi: 10.1016/j.jvolgeores.2005.07.013.
Newman, A.V., Malin, P.E., Ellsworth, W., Hill, D.P., Julian, B.R., 1997. Fluid pulsations in the Casa Diablo area, Mammoth, CA? EOS Trans. Am. Geophys. Union 78 (46), F431 (abstract).
Newman, A.V., Dixon, T.H., Ofoegbu, G., Dixon, J.E., 2001. Geodetic and seismic constraints on recent activity at Long Valley caldera, California: evidence for viscoelastic rheology. J. Volcanol. Geotherm. Res. 105, 183–206.
Prejean, S., Stork, A., Ellsworth, W., Hill, D., Julian, B., 2003. High precision earthquake locations reveal seismogenic structure beneath Mammoth Mountain, California. Geophys. Res. Lett. 30 (24), doi: 10.1029/2003GL018334 (SDE 4:1-4).
Press, W.H., Teukolsky, S.A., Vetterling, W.T., Flannery, B.P., 1992. Numerical Recipes in FORTRAN. Cambridge University Press, New York, NY, USA.
Sanders, C.O., Nixon, L.D., 1995. S wave attenuation structure in Long Valley caldera, California from three-component S to P amplitude ratio data. J. Geophys. Res. 100, 12395–12404.
Sanders, C.O., Ponko, S.C., Nixon, L.D., Schwartz, E.A., 1995. Seismological evidence for magmatic and hydrothermal structure in Long Valley caldera from local earthquake attenuation and velocity tomography. J. Geophys. Res. 100, 8311–8326.
Savage, J.C., Cockerham, R.S., 1984. Earthquake swarm in Long Valley caldera, California, January 1983: evidence for dike inflation. J. Geophys. Res. 89, 8315–8324.
Savage, J.C., Cockerham, R.S., Estrem, J.E., Moore, L.R., 1987. Deformation near Long Valley caldera, eastern California, 1982–1986. J. Geophys. Res. 92, 2721–2746.
Sella, G., Dixon, T., Mao, A., 2002. REVEL: a model for recent plate velocities from space geodesy. J. Geophys. Res. 107 (B4), doi: 10.1029/2000JB000033 (ETC 11 1–31).
Slater, L., Huggett, G.R., 1977. A multi-wavelength-distance-measuring instrument for geophysical experiments. J. Geophys. Res. 81, 6299–6306.
Sorey, M.L., Suemnicht, G.A., Sturchio, N.C., Nordquist, G.A., 1991. New evidence on the hydrothermal system in Long Valley caldera, California, from wells, fluid sampling, electrical geophysics, and age determinations of hot-spring deposits. J. Volcanol. Geotherm. Res. 48, 229–263.
Steck, L.K., Prothero, W.A., 1994. Crustal structure beneath Long Valley caldera from modeling of teleseismic P-wave polarizations and Ps converted waves. J. Geophys. Res. 99, 6881–6898.
Thatcher, W., Massonnet, D., 1997. Crustal deformation at Long Valley caldera, eastern California. Geophys. Res. Lett. 24, 2519–2522.
Tiampo, K.F., Rundle, J.B., Fernandez, J., Langbein, J.O., 2000. Spherical and ellipsoidal volcanic sources at Long Valley cal-

dera, California, using a genetic algorithm inversion technique. J. Volcanol. Geotherm. Res. 102, 189–206.

Vogel, T.A., Eichelberger, J.C., Younker, L.W., Schuraytz, B., Horkowitz, J., Stockman, H., Westrich, H., 1989. Petrology and emplacement of intrusive and extrusive rhyolites of Obsidian Dome, Inyo Craters volcanic chain, eastern California. J. Geophys. Res. 94, 17937–17956.

Webb, F., Birsik, M., Dixon, T., Farina, F., Stein, R., Marshall, G., 1995. Inflation of Long Valley caldera from on year of continuous GPS measurements. Geophys. Res. Lett. 22, 195–198.

Wessel, P., Smith, W., 1998. New, improved version of generic mapping tools released. Trans. Am. Geophys. Union (EOS) 79, 579.

Yang, X.-M., Davis, P.M., Dietrich, J.H., 1988. Deformation from inflation of a dipping finite prolate spheroid in an elastic half-space as a model for volcanic stressing. J. Geophys. Res. 93 (B5), 4249–4257.